ACS OMEGA

Open Access

http://pubs.acs.org/journal/acsodf

Article

Geochemical Characteristics and Uranium Mineralization Processes in the Shawan Formation of the Chepaizi Uplift, Junggar Basin, Northwestern China

Niannan Chen, Mangen Li,* Guangzhen Mao, Xiangfei Tang, Shengming Wu, Jianbing Duan, Baowen Guan, Pengfei Fan, Rui Jin, and Jin Wang

Cite This: *ACS Omega* 2024, 9, 48681−48696

Read Online

ACCESS | Metrics & More | Article Recommendations

ABSTRACT: The Chepaizi Uplift, situated on the western edge of the Junggar Basin in northwestern China, has recently become a significant target area for in situ leach sandstone-type uranium exploration. The Neogene Shawan Formation, a newly identified uranium-bearing layer, has gained considerable attention for its potential. This study utilizes scanning electron microscopy (SEM), X-ray powder diffraction (XRD), whole-rock geochemistry, and electron probe microanalysis (EPMA) of uranium minerals. Combined with sedimentological and tectonic background analysis, these methods were applied to investigate geochemical characteristics and uranium mineralization processes. The sandstones in the Shawan Formation are primarily lithic sandstone and subarkose, with the provenance dominated by felsic rocks from the upper crust. Coffinite is the predominant uranium mineral, accompanied by titanium−uranium oxides and minor amounts of pitchblende. Coffinite appears as colloidal coatings around framboidal pyrite, in short-prismatic aggregates corroding albite, and as banded structures within calcite cement. Elemental ratios indicate that the Shawan Formation's paleo-hydrological environment was arid, continental, and brackish, with paleo-redox conditions reflecting a hot, dry climate. Uranium mineralization occurred in two stages: initially, uranium-containing oxygenated waters migrated laterally across slope zones, forming a redox transition zone and resulting in the pre-enrichment of uranium. Subsequently, hydrocarbons migrated along faults and unconformities, leading to secondary reduction of the interlayer oxidation zone and resulting in uranium enrichment and mineralization at the interface of grayish-green and gray sandstone layers.

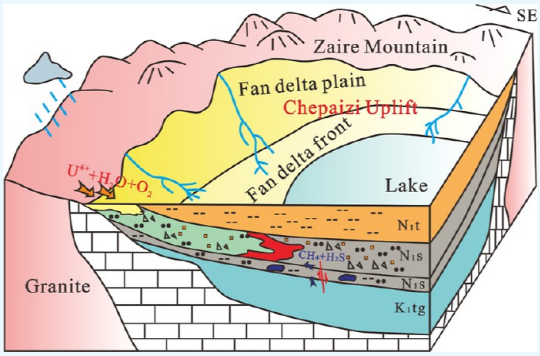

1. INTRODUCTION

Sandstone-type uranium deposits are characterized by their large scale, economic viability, and ease of extraction, making them the most widely utilized type of uranium deposit globally. The Junggar Basin, a large basin in northern China with rich coal, oil, and gas resources, is also a key area for in situ leach sandstone-type uranium exploration.[1] Since the Cenozoic era, the Junggar Basin has been in a relatively stable sedimentary state, resulting in the formation of extensive sedimentary slope belts along its margins. Furthermore, the region has experienced arid to semiarid climatic conditions since the Neogene, providing favorable structural and climatic conditions for sandstone-type uranium mineralization.[2,3]

Currently, geological party no. 216 (China National Nuclear Corporation, CNNC) has made successive discoveries of interlayer oxidation zones and associated industrial uranium ore bodies in various regions of the Junggar Basin, including the Kamust area,[4−6] the Beisantai area,[7−10] and the Jiangjunmiao area in the east,[11,12] as well as in the Dingshan area in the north[13−15] and the Louzhuangzi area in the south.[16−19] However, research on the western margin of the Junggar Basin is relatively underdeveloped, and no breakthroughs have been made in prospecting efforts. Substantial natural gamma anomaly boreholes were discovered during oil exploration by China National Petroleum Corporation and Sinopec Group in the Chepaizi Uplift in the western Junggar Basin,[20,21] with high natural gamma anomalies primarily found in the Neogene Shawan Formation conglomerates and gristone.[22] This indicates a promising prospect for mineral exploration in this area. Thus, the Chepaizi Uplift is not only a key area for oil extraction but also a promising region for sandstone-type uranium exploration. The potential for sand-

Received: August 25, 2024
Revised: November 9, 2024
Accepted: November 20, 2024
Published: November 28, 2024

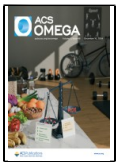

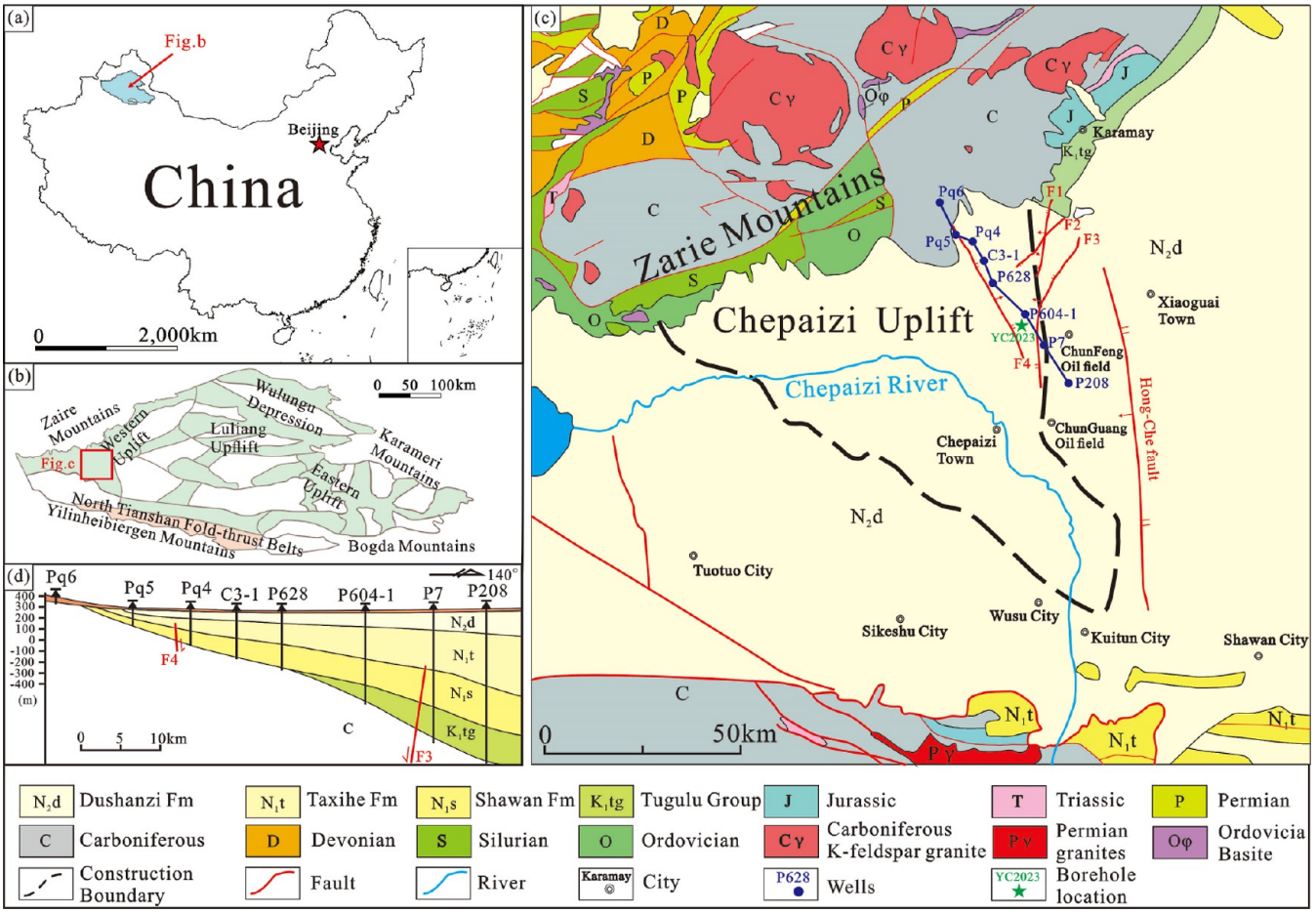

Figure 1. Division of structural units in the Junggar basin and geological sketch of Chepaizi Uplift (Revised from Mao et al.[27]) Adapted with permission from ref 27. Copyright: [Uranium Geology, 2023].

stone-type uranium mineralization in this area warrants further analysis and research.

Currently, scholars have extensively studied the distribution of sand bodies in the Chepaizi Uplift since the Neogene and their influence on hydrocarbon accumulation patterns. Most existing research focuses on sedimentary structures,[22,23] tectonic evolution,[24] hydrogeochemical characteristics,[25] and the assessment of mineralization potential.[26,27] However, research on the formation mechanisms of sandstone-hosted uranium deposits in this area is relatively lacking, limiting breakthroughs in the exploration of such deposits in the Chepaizi Uplift. Therefore, this research focuses on the newly discovered industrial uranium boreholes in the Neogene Shawan Formation of the Chepaizi Uplift. Through petrological, mineralogical, and geochemical methods, this research systematically analyzes the properties of the Shawan Formation sandstone parent rocks, tectonic background, and uranium mineral characteristics, providing a basis for understanding the metallogenic mechanisms of Neogene sandstone-type uranium deposits in the Chepaizi Uplift of the Junggar Basin.

2. GEOLOGICAL SETTING

The Junggar Basin, located in northwest China, is rich in multiple energy resources such as oil, gas, and coal (Figure 1a). The Junggar Block belongs to the Paleo-Asian Ocean tectonic domain, and the Junggar Basin mainly consists of six structural units: the Western Uplift, the Ulungur Depression, the Luliang Uplift, the Central Depression, the Eastern Uplift, and the Northern Tianshan Fold and Thrust Belt (Figure 1b).[28−32] The Chepaizi Uplift is situated on the western edge of the Junggar Basin, with a length of approximately 100 km from north to south and a width of 20−95 km from east to west, forming an inverted irregular triangle (Figure 1c). The southern part of the Chepaizi Uplift is adjacent to the Sikeshu Depression, the northern part borders the Zaire Mountain, and the eastern part connects to the Shawan Depression.[24] The Chepaizi Uplift trends northwest-southeast, with uneven internal uplift. The northwestern part, near the front of Zaire Mountain, exhibits the highest uplift, gradually decreasing toward the southeast, forming a gently southward-dipping monocline (Figure 1d).[26] The average leaching rate of active uranium in the exposed K-feldspar granite of Zaire Mountain is 2.62%. Additionally, since the Neogene, alternating wet and dry climates and tectonic movements during the Yanshanian and Himalayan periods have intensified groundwater circulation. These factors provide the Chepaizi Uplift with the necessary conditions for forming sandstone-type uranium deposits, including a rich uranium source, a large-scale slope belt, a favorable groundwater recharge-flow-discharge system, and a suitable redox environment.[27]

The stratigraphy of the Chepaizi Uplift includes the Lower Cretaceous Tugulu Group (K_1tg), the Neogene Shawan Formation (N_1s), Taxihe Formation (N_1t), Dushanzi Formation (N_2d), and Quaternary sediments (Q) (Figure 1d).

https://doi.org/10.1021/acsomega.4c07825
ACS Omega 2024, 9, 48681−48696

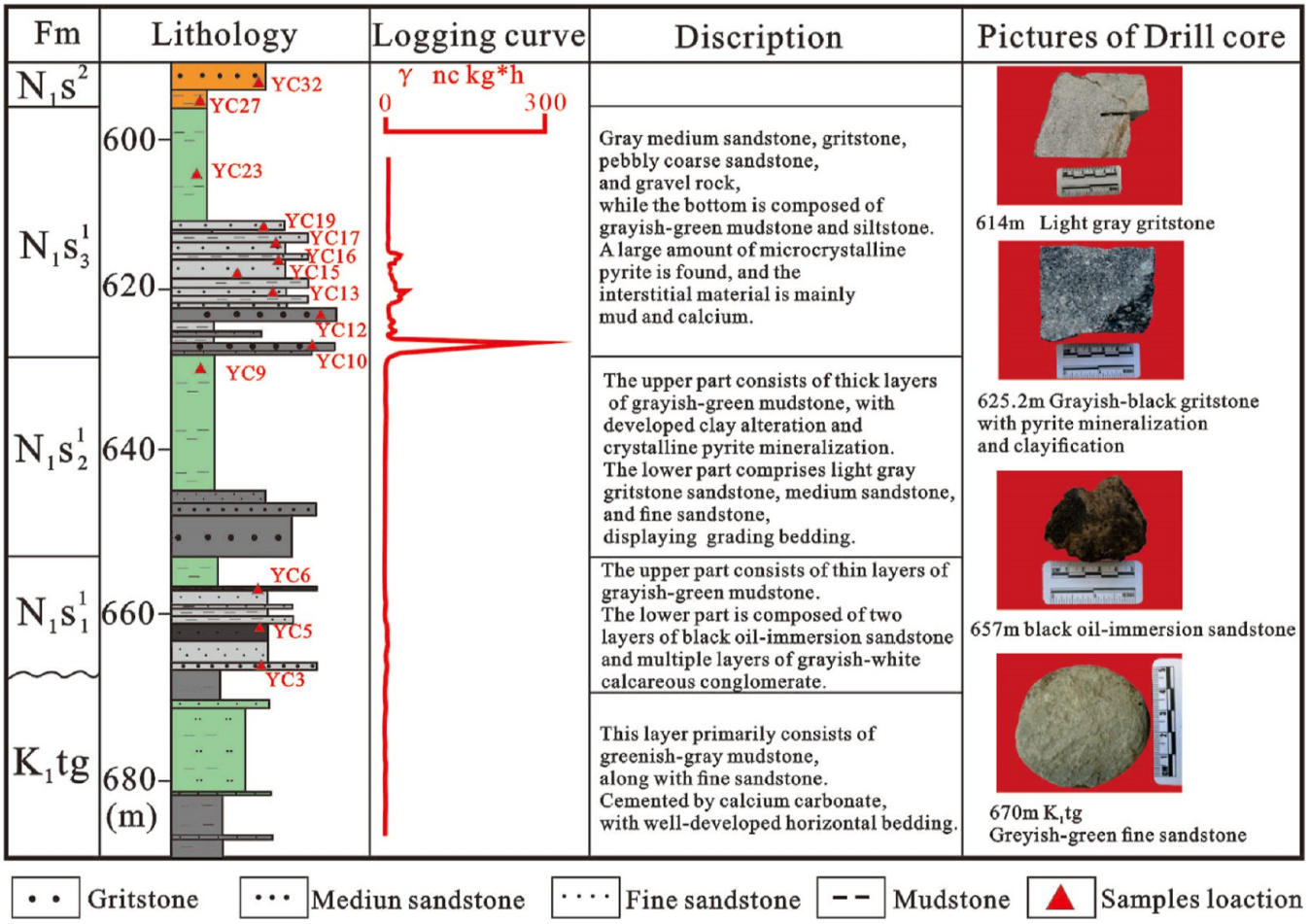

Figure 2. Comprehensive diagram of YC2023 borehole in Chepaizi Uplift.

The uranium-bearing target layer is the Neogene Shawan Formation, which can be further subdivided into the first (N_1S_1), second (N_1S_2), and third (N_1S_3) members. The first member (N_1S_1) is divided from bottom to top into three sand groups.[30,31] The first sand group ($N_1S_1^1$) mainly consists of thick layers of conglomerate, gritstone, medium sandstone and fine sandstone, with occasional thin mudstone interbeds. The second sand group ($N_1S_1^2$) is primarily composed of thick mudstone layers. The third sand group ($N_1S_1^3$) mainly consists of thick conglomerate layers and exhibits a significant uranium-induced gamma-ray anomaly (Figure 2).

3. SAMPLES AND ANALYTICAL METHODS

3.1. Sample Collection and Petrographic Analysis. Fourteen samples were collected from well YC2023 in the Chepaizi Uplift, with the sampling interval taken from fresh core samples of the Shawan Formation at a depth of 580 to 680 m. The lithology primarily consists of gray gritstone, medium sandstone, grayish-green fine sandstone and mudstone, black oil-impregnated sandstone, and light brown conglomerate. The samples were sent to Nanjing Mineral Exploration Technology Co., Ltd. for thin section preparation. Microscopic petrographic observations and clastic grain composition analysis were conducted at the Basic Geology Laboratory of the School of Earth Sciences, East China University of Technology. The microscope used in this study was a Zeiss AxioImager M2m.

3.2. XRD, SEM and EPMA Analyses. The X-ray powder diffraction (XRD) analysis and uranium mineral morphology studies for this research were completed in the Scanning Electron Microscope Laboratory of the State Key Laboratory of Nuclear Resources and Environment at East China University of Technology. The XRD analysis was conducted using a Bruker D8 ADVANCE X-ray diffractometer, with a relative deviation of less than 20% for the content of each mineral in the samples and less than 10% for clay minerals. The Cu target X-ray tube operated at a voltage of ≤40 kV and a current of ≤40 mA, with the goniometer set in the θ/θ mode. The scanning range was 5−80°, with a goniometer precision of 0.0001° and an accuracy of ≤0.02°. The scanning electron microscope (SEM) used was a Zeiss Gemini Sigma 300 VP SEM, operating at an acceleration voltage of 20 V to 30 kV. The microchemical composition of uranium minerals was analyzed using an electron probe (EPMA) at the State Key Laboratory of Nuclear Resources and Environment, East China University of Technology. The equipment used was a JXA-8530F electron probe coupled with an Inca Energy spectrometer. The testing conditions were as follows: an acceleration voltage of 15.0 kV, a probe current of 20.0 nA, and a beam spot diameter of <2 μm. All testing processes strictly adhered to the national standard GB/T 15617-2002.[33]

3.3. Geochemical Analysis of Whole Rock Elements. The major and trace element compositions were determined by X-ray fluorescence (XRF-1800; SHIMADZU) on fused glasses and inductively coupled plasma mass spectrometry

https://doi.org/10.1021/acsomega.4c07825
ACS Omega 2024, 9, 48681−48696

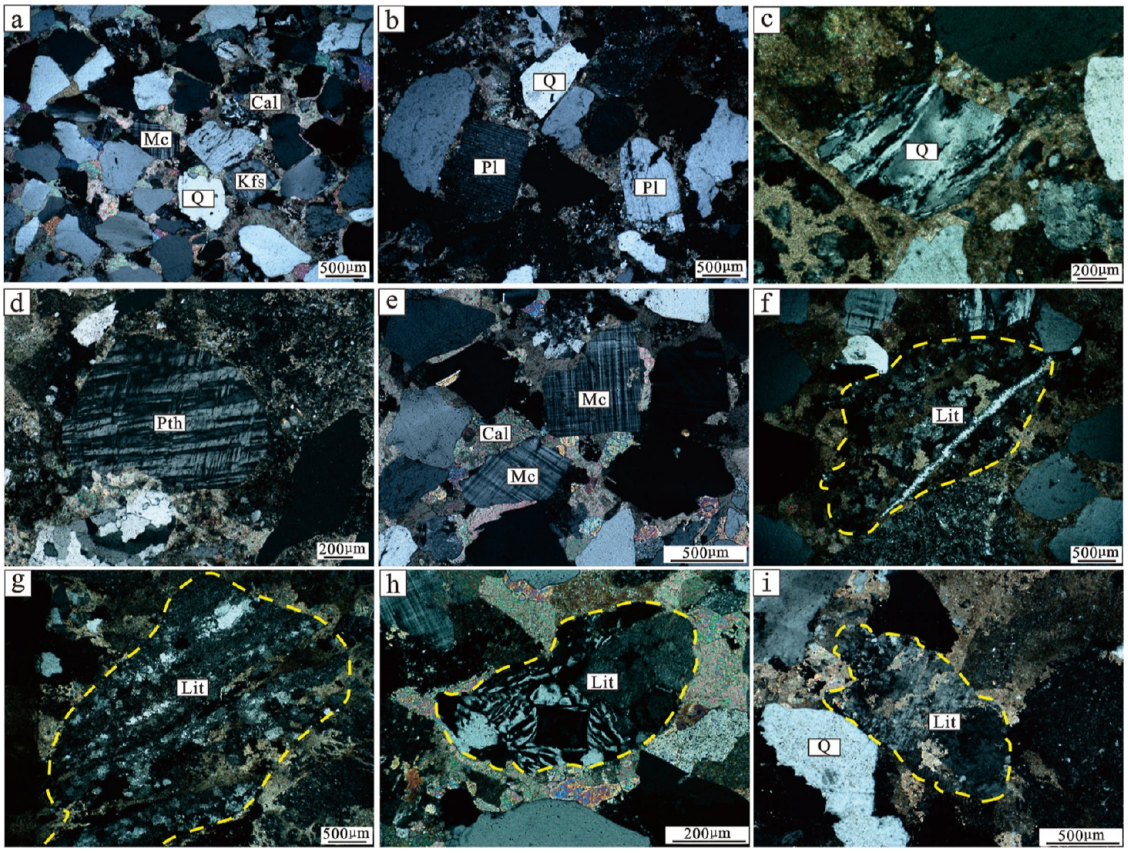

Figure 3. Photomicrographs showing the typical sandstone samples from Shawan Formation in Chepaizi Uplift. (a) Medium to coarse-grained sandstone of the Shawan Formation. (b) Plagioclase single crystal with illitization on the surface. (c) Quartz crystal displaying undulatory extinction. (d) Perthite crystal. (e) Microcline with well-developed grid twinning. (f) Fine-grained granite lithic fragment. (g) Rhyolite rock fragment with flow structure. (h) Granite breccia with a cataclastic texture. (i) Granite lithic fragment with calcite dissolution along the edges and interior. Q: Quartz; Mc: Microcline; Kfs: K-feldspar.; Pl: Plagioclase; Pth: perthite; Cal: Calcite; Lit: lithic fragments.

(PlasmaQuant MS; Analytikjena) after acid digestion of samples in Teflon bombs, at Createch Testing Tianjin Technology Co., Ltd. Loss on ignition was measured after heating to 1000 °C for 3 h in a muffle furnace. The precision of the XRF analyses is within ±2% for the oxides greater than 0.5 wt % and within ±5% for the oxides greater than 0.1 wt %. Sample powders (about 50 mg) were dissolved in Teflon bombs using a HF + HNO_3 mixture for 48 h at about 190 °C. The solution was evaporated to incipient dryness, dissolved by concentrated HNO_3 and evaporated at 150 °C to dispel the fluorides. The samples were diluted to about 100 g for analysis after redissolved in 30% HNO_3 overnight. An internal standard solution containing the element Rh was used to monitor signal drift during analysis. Analytical results for USGS standards indicated that the uncertainties for most elements were within 5%.

4. RESULTS

4.1. Petrography and Mineralogy. The sandstones of the Shawan Formation can be divided into fine sandstones, medium sandstones, and gritstone based on grain size. The sandstones exhibit moderate sorting, poor roundness, and are commonly cemented by calcite. The composition mainly includes quartz, feldspar, lithic fragments, biotite, muscovite, and pyrite (Figure 3a). The quartz grains in the Shawan Formation have relatively smooth surfaces, with embayed edges caused by dissolution (Figure 3b) and exhibit undulatory extinction (Figure 3c). Feldspar primarily consists of plagioclase (Figure 3d) and microcline (Figure 3e). The lithic fragments are mainly derived from fine-grained granite (Figure 3f) and rhyolite (Figure 3g), with rhyolitic fragments developing flow structures and a few granitic breccias showing graphic textures (Figure 3h). Some lithic fragments have edges or interiors that have become indistinct due to calcite dissolution (Figure 3i).

4.2. XRD Analysis Results. X-ray diffraction analysis was performed on selected samples from different layers of the Shawan Formation, including oil-immersion sandstones (YC5, YC6), uranium-bearing sandstones (YC12, YC15, YC16), nonmineralized sandstones (YC21, YC24, YC25), and oxidized conglomerates (YC34). The main minerals in the Shawan Formation of the Chepaizi Uplift are K-feldspar, microcline, quartz, muscovite, calcite, and some clay minerals. In the lower reduced zone, the quartz content in the oil-immersion sandstones range from 55.39% to 59.44%, with an average of 57.42%. Muscovite content ranges from 2.66% to 6.10%, with an average of 4.38%, and there are trace amounts of calcite and K-feldspar. In uranium-bearing sandstones, the quartz content ranges from 50.23% to 59.47%, with an average of 54.55%. These sandstones are generally cemented by calcite, with calcite content ranging from 16.86% to 21.87%, averaging 19.73%. The K-feldspar content ranges from 13.32% to 20.18%, with an average of 16.16%. There is also a small amount of Illite present, ranging from 2.73% to 4.3%, with an average of 2.73%. In nonmineralized sandstones, the quartz

https://doi.org/10.1021/acsomega.4c07825
ACS Omega 2024, 9, 48681−48696

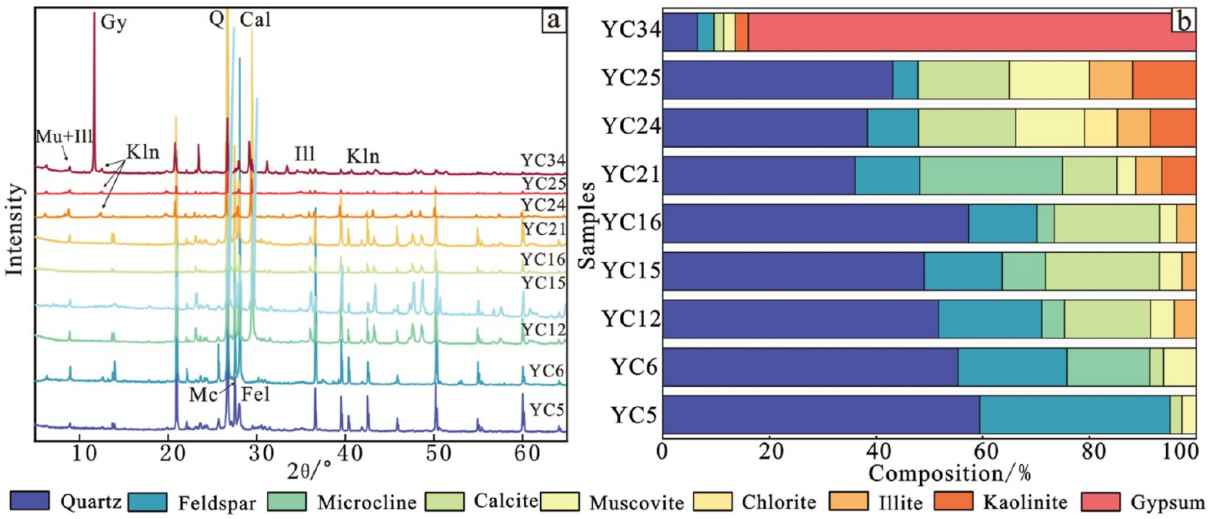

Figure 4. XRD analysis patterns of samples from different depths in the Shawan Formation. (a) Patterns of mineral composition variation. (b) Relative mineral content. Qtz: Quartz; Fel: Feldspar; Mu: Muscovite; Kln: Kaolinite; Mc: Microcline; Cal: Calcite; Chl: Chlorite; Ill: Illite; Gy: Gypsum.

content is relatively lower, ranging from 36.04% to 43.11%, with an average of 39.18%. The K-feldspar content is also lower than in mineralized sandstones, ranging from 4.73% to 12.14%, with an average of 8.81%. Illite content ranges from 4.91% to 8.09%, with an average of 6.38%, and kaolinite content ranges from 6.41% to 11.9%, with an average of 8.98%. In the upper oxidized zone, the quartz content in the conglomerate is only 6.46%, but the gypsum content is high at 83.93%. The XRD analysis results indicate that as depth decreases from deep to shallow, the degree of weathering in the Shawan Formation increases. The content of weathering-resistant minerals such as K-feldspar and microcline gradually decreases, while the amount of clay minerals increases. The dominant clay mineral type shifts from Illite to kaolinite (Figure 4).

4.3. Major Element Characteristics. The SiO_2 content in the Shawan Formation samples from the Chepaizi Uplift ranges from 43.89% to 89.76%, with an average of 58.74%. The CaO content ranges from 0.47% to 23.02%, with an average of 13.95%. The Al_2O_3 content varies between 4.03% and 17.28%, with an average of 7.66%. K_2O content ranges from 1.44% to 2.78%, with an average of 1.9%. Na_2O content ranges from 0.87% to 2.33%, with an average of 1.3%. MgO content ranges from 0.14% to 3.58%, with an average of 0.14%. TiO_2 content varies between 0.1% and 0.88%, with an average of 0.29%. Fe_2O_3 content ranges from 0.07% to 5.77%, with an average of 1.75%. FeO content ranges from 0.1% to 2.4%, with an average of 0.64%. P_2O_5 content ranges from 0.02% to 0.21%, with an average of 0.06%. MnO content ranges from 0.01% to 0.15%, with an average of 0.05%. The combined $Na_2O + K_2O$ content ranges from 2.32% to 4.74%, with an average of 3.2%. The K_2O/Na_2O ratio ranges from 1.03% to 1.7%, with an average of 1.49% (Table 1).

4.4. Trace Element and Rare Earth Element Characteristics. The trace element concentrations of 14 samples from different zones of the Chepaizi Uplift are shown in Table 2. The large ion lithophile elements (LILEs) Rb, Sr, and Ba in the Shawan Formation show a slight depletion relative to the upper continental crust.[36] In contrast, the high field strength elements (HFSEs) Y, Nb, Zr, and Th exhibit similar distribution characteristics, with average contents close to those of the upper continental crust (Figure 5a).

The total rare earth element (ΣREE) content in the Shawan Formation sandstones ranges from 16.5 to 170.45 ppm, with an average of 61.61 ppm. The light rare earth elements (LREEs) range from 13.99 to 154.97 ppm, with an average of 54.08 ppm, while the heavy rare earth elements (HREEs) range from 2.3 to 18.25 ppm, with an average of 7.53 ppm, showing a clear enrichment in REEs. The LREE/HREE ratio varies between 4.31 and 10.1 ppm, with an average of 6.69 ppm, indicating significant LREE enrichment, HREE depletion, and a high degree of differentiation between LREEs and HREEs. The LREE fractionation coefficient $(La/Sm)_N$ ranges from 2.1 to 5.08 ppm, with an average of 3.57 ppm. In comparison, the HREE fractionation coefficient $(Gd/Yb)_N$ ranges from 0.86 to 1.75 ppm, with an average of 1.33 ppm, indicating that LREE fractionation is higher than that of HREEs. The chondrite-normalized REE distribution curves show a slightly right-leaning "V" shape with moderate negative Eu anomalies (Figure 5b). The parallel distribution patterns of the REE curves across different samples suggest a similar and relatively stable source of material.

4.5. Chemical Compositions of Uranium Minerals. In the uranium-bearing sandstones of the Shawan Formation within the Chepaizi Uplift, the primary uranium mineral is coffinite, followed by smaller amounts of pitchblende and titanium−uranium oxides (Table 3). The UO_2 content in coffinite ranges from 55.23% to 65.27%, averaging 61.81%. The SiO_2 content ranges between 6.18% and 12.58%, with an average of 8.88%. The CaO content varies from 1.91% to 7.67%, averaging 4.6%. The MoO_3 content ranges from 1.11% to 3.48%, with an average of 2.33%. Compared to pitchblende, coffinite generally exhibits a lower UO_2 content, higher SiO_2 content, and relatively stable CaO content. In pitchblende, the UO_2 content ranges from 80.62% to 85.49%, averaging 83.03%. The SiO_2 content is between 0.61% and 1.61%, averaging 1.09%. The CaO content ranges from 0.03% to 4.92%, with an average of 2.21%. Overall, pitchblende shows higher UO_2 content and lower SiO_2 and CaO content. Titanium−uranium oxides have UO_2 content ranging from 43.44% to 58.72%, with an average of 53.03%. Their SiO_2

https://doi.org/10.1021/acsomega.4c07825
ACS Omega 2024, 9, 48681−48696

Table 1. Analysis Results of Major Elements in the Sandstone Samples from the Shawan Formation[a]

sample	grayish-green zone		black oil zone		light gray uranium mineralized zone								light brown zone		upper crust
	YC3	YC23	YC5	YC6	YC9	YC10	YC12	YC13	YC15	YC16	YC17	YC19	YC27	YC32	
SiO_2	55.70	55.43	86.71	87.76	46.72	64.86	55.32	62.97	47.76	58.23	47.48	54.92	43.89	54.65	65.89
Al_2O_3	5.44	17.28	7.55	6.22	12.31	4.93	5.01	4.06	5.66	4.03	6.07	4.09	12.48	12.17	15.17
K_2O	1.64	2.78	2.25	2.32	2.40	1.65	1.57	1.53	1.44	1.45	1.53	1.45	2.17	2.41	3.39
Na_2O	1.22	1.75	1.39	1.45	1.45	1.25	0.92	0.96	1.23	0.89	1.22	0.87	1.30	2.33	3.89
CaO	19.11	1.92	0.47	0.56	10.33	13.36	20.51	17.11	22.94	19.68	23.02	20.51	15.17	10.67	4.19
TiO_2	0.18	0.88	0.10	0.10	0.65	0.22	0.13	0.12	0.20	0.10	0.19	0.11	0.60	0.50	0.5
MnO	0.04	0.08	0.01	0.01	0.08	0.14	0.02	0.02	0.02	0.02	0.03	0.0	0.15	0.09	0.07
MgO	0.43	3.58	0.14	0.16	1.19	0.25	0.31	0.24	0.44	0.28	0.47	0.43	2.43	1.61	0.2
P_2O_5	0.04	0.06	0.03	0.03	0.21	0.04	0.02	0.02	0.02	0.02	0.02	0.02	0.15	0.10	0.2
$Fe_2O_3^T$	0.80	6.85	0.27	0.37	7.51	0.38	0.32	0.25	1.38	0.25	1.31	1.08	5.18	5.04	
Fe_2O_3	0.39	4.94	0.07	0.24	5.77	0.15	0.15	0.11	1.06	0.17	0.70	0.67	5.36	4.66	
FeO	0.45	2.40	0.20	0.16	2.32	0.25	0.18	0.15	0.43	0.10	0.67	0.47	0.36	0.85	
FeO/Fe_2O_3	0.88	2.06	0.37	1.51	2.49	0.59	0.85	0.70	2.47	1.65	1.04	1.43	14.92	5.48	
LOI	15.02	8.61	0.74	0.85	10.80	10.79	15.92	13.27	17.73	15.40	17.83	15.91	16.43	11.29	
total	99.60	99.23	99.65	99.83	93.66	97.86	100.1	100.5	98.83	100.3	99.17	99.41	99.95	100.8	
CIA	57.20	73.35	60.00	54.36	69.89	54.33	59.49	54.00	59.19	55.51	60.45	56.15	72.37	63.26	
ICV	4.23	0.92	0.59	0.78	1.78	3.45	4.71	4.95	4.83	5.60	4.48	5.88	2.18	1.83	
F1	4.25	−1.65	−6.43	−7.22	5.31	0.28	4.68	2.15	7.37	3.75	7.47	4.67	5.07	3.65	
F2	5.41	−3.69	−1.05	−0.96	1.14	3.25	5.70	4.24	6.69	5.08	6.85	5.05	1.86	2.66	
F3	5.20	−2.17	4.96	7.73	−4.36	7.60	5.80	8.50	2.57	7.69	2.53	5.27	−2.16	−1.04	
F4	−0.60	0.63	−2.19	−1.79	−4.93	−0.12	−0.66	−0.34	−1.58	−0.22	−1.56	−1.28	−0.05	−1.73	

[a]Chemical index of alteration (CIA) = $100*Al_2O_3/(Al_2O_3 + CaO* + Na_2O + K_2O)$. The chemical composition of the formula is the mole number, CaO* is only the CaO in silicate minerals, and because silicate is not easy to dissolve, the more accurate value of CaO in the source area is preserved. In this paper, the correction method proposed by McLennan was adopted for CIA calculation, i.e., according to the average composition of Na and Cain natural silicate minerals and the mole ratio of CaO/NaO in sediment samples; if the CaO mole is greater than Na_2O, Na_2O mole is used as CaO mole, otherwise, the CaO mole is used.[34] $F1 = -1.773TiO_2 + 0.607Al_2O_3 + 0.76Fe_2O_3^T - 1.5MgO + 0.616CaO + 0.509Na_2O - 1.224K_2O - 0.909$.[34] $F2 = 0.445TiO_2 + 0.07Al_2O_3 - 0.25Fe_2O_3^T - 1.142MgO + 0.438CaO + 1.475Na_2O + 1.426K_2O - 6.861$.[34] $F3 = (30.638TiO_2 - 12.541Fe_2O_3^T + 7.329MgO + 12.031Na_2O + 35.402K_2O)/Al_2O_3 - 6.382$.[34] $F4 = (36.5TiO_2 - 10.879Fe_2O_3^T + 30.875MgO - 5.404Na_2O + 11.112K_2O)/Al_2O_3 - 3.89$.[34] Index of compositional variability (ICV) = $(Fe_2O_3 + K_2O + Na_2O + CaO + MgO + MnO + TiO_2)/Al_2O_3$.[35]

https://doi.org/10.1021/acsomega.4c07825
ACS Omega 2024, 9, 48681−48696

Table 2. Analysis Results of Trace and Rare Earth Elements in Sandstone of the Shawan Formation[a]

samples	grayish-green zone		black oil zone		light gray uranium mineralized zone								light brown zone	
	YC3	YC23	YC5	YC6	YC9	YC10	YC12	YC13	YC15	YC16	YC17	YC19	YC27	YC32
Li	9.88	88.74	3.23	4.57	38.42	6.37	6.14	5.09	10.24	7.22	16.78	7.31	40.64	27.14
Be	2.82	2.92	1.37	1.20	2.50	1.85	1.54	1.54	1.28	1.86	1.37	2.39	1.97	1.84
Sc	3.23	19.12	0.60	0.77	20.12	1.78	1.59	1.55	3.16	1.80	4.03	1.65	13.90	11.14
V	16.99	121.20	4.97	6.07	133.20	15.96	10.18	12.71	19.18	13.26	21.42	9.86	97.14	80.22
Cr	9.41	97.23	4.96	4.50	78.31	16.08	6.17	7.67	14.60	10.19	36.77	32.77	64.79	83.46
Mn	306.1	657.1	55.95	48.47	601.9	1064.1	197.3	163.3	189.2	190.1	259.7	72.3	1139.9	691.9
Co	1.41	20.46	0.46	0.52	37.98	1.15	2.82	1.04	2.26	0.38	1.50	0.75	11.80	8.40
Ni	6.20	50.82	1.88	2.17	95.45	4.91	2.7	2.32	7.14	1.29	7.87	13.45	37.56	40.16
Cu	3.17	38.39	1.40	1.44	52.29	2.68	4.63	1.52	3.53	2.82	3.72	3.25	32.81	25.31
Zn	11.06	120.7	8.03	9.09	147.20	9.29	9.30	6.35	8.70	6.15	13.65	6.61	79.83	60.74
Ga	5.22	22.46	5.20	4.64	26.55	6.60	5.07	4.21	5.72	3.62	6.50	3.76	15.87	14.86
Rb	51.44	151.9	70.84	65.78	95.79	51.16	49.79	48.41	48.19	46.29	59.70	45.23	89.30	77.83
Sr	429.7	231.7	85.5	89.1	1469.6	474.9	274.9	166.8	296.9	183.6	304.1	278.8	238.6	241.9
Hf	1.71	5.19	3.59	1.36	4.98	2.44	2.97	1.53	1.71	1.45	1.56	1.57	4.07	4.44
Ta	0.56	1.26	0.10	0.13	0.85	0.19	0.19	0.10	0.31	0.13	0.38	0.13	0.71	0.52
W	0.46	3.60	0.38	0.32	2.91	2.13	0.33	0.35	0.60	0.21	0.98	0.65	1.87	1.63
Tl	0.27	0.86	0.36	0.36	0.68	0.21	0.27	0.26	0.27	0.25	0.31	0.23	0.48	0.38
Pb	8.35	22.46	10.96	10.54	27.74	7.94	7.89	7.45	11.63	7.8	11.62	6.19	20.17	16.77
Th	1.99	13.02	1.49	1.62	10.20	1.85	2.80	1.49	1.81	1.93	2.74	1.95	9.06	6.18
U	22.91	8.03	0.61	0.66	177.7	1902.1	28.19	127.1	28.81	32.80	96.90	30.61	1.91	1.59
Zr	58.80	164.75	129.2	46.92	164.2	107.13	103.1	48.83	56.45	47.43	51.80	54.20	126.1	148.8
Nb	3.84	17.68	1.40	1.59	12.33	3.57	2.07	1.45	3.68	1.43	4.50	1.87	10.92	7.86
Mo	1.35	3.05	0.35	0.23	461.8	3818.2	10.06	27.54	13.78	9.05	44.78	76.65	1.17	1.73
Sn	0.88	4.28	0.38	0.39	3.21	7.61	0.51	0.72	0.97	0.65	1.39	0.85	2.59	1.96
Cs	1.78	14.83	2.25	2.10	8.71	2.10	1.83	1.79	2.08	1.60	2.84	1.83	8.20	5.50
Ba	303.7	393.8	268.5	274.7	486.4	403.3	197.8	193.2	204.2	201.6	195.2	200.4	510.6	653.7
La	10.18	33.44	4.92	6.21	34.54	3.91	5.82	5.71	5.16	3.71	7.71	4.08	29.44	23.47
Ce	19.42	62.25	10.18	12.49	66.98	7.73	11.29	12.06	9.00	6.36	16.52	6.24	47.71	39.50
Pr	2.32	8.34	0.87	1.22	9.22	0.81	1.29	1.52	0.99	0.61	1.78	0.54	6.90	5.64
Nd	9.53	31.39	3.81	5.10	36.04	3.59	5.51	7.65	4.36	2.80	7.37	2.47	26.16	22.10
Sm	1.92	6.18	0.76	1.00	6.87	0.82	1.15	1.75	0.91	0.58	1.51	0.52	5.17	4.55
Eu	0.48	1.20	0.23	0.29	1.33	0.18	0.26	0.48	0.25	0.15	0.38	0.13	1.10	1.05
Gd	1.73	5.15	0.70	0.88	4.80	0.74	1.11	1.88	0.95	0.56	1.37	0.57	4.62	4.14
Tb	0.29	0.93	0.11	0.13	0.82	0.14	0.19	0.32	0.16	0.08	0.23	0.09	0.81	0.73
Dy	1.60	4.73	0.64	0.76	3.89	0.90	1.15	1.78	1.00	0.56	1.32	0.67	4.15	3.82
Ho	0.35	1.05	0.14	0.16	0.82	0.20	0.28	0.39	0.24	0.13	0.31	0.16	0.93	0.86
Er	0.96	2.84	0.40	0.45	2.20	0.61	0.82	1.05	0.71	0.39	0.88	0.49	2.49	2.33
Tm	0.14	0.41	0.06	0.07	0.33	0.10	0.12	0.15	0.11	0.06	0.13	0.08	0.36	0.33
Yb	0.93	2.73	0.41	0.47	2.27	0.71	0.86	1.04	0.73	0.44	0.89	0.55	2.37	2.22
Lu	0.14	0.42	0.06	0.07	0.35	0.11	0.14	0.16	0.11	0.07	0.14	0.09	0.37	0.35
Y	10.41	27.55	6.18	3.98	20.76	6.56	10.00	9.57	7.76	4.02	9.57	4.71	25.60	23.93
ΣREE	50.0	161.1	23.28	29.29	170.4	20.54	29.96	35.93	24.66	16.51	40.54	16.68	132.5	111.1

https://doi.org/10.1021/acsomega.4c07825
ACS Omega 2024, 9, 48681−48696

Table 2. continued

samples	grayish-green zone		black oil zone		light gray uranium mineralized zone								light brown zone	
	YC3	YC23	YC5	YC6	YC9	YC10	YC12	YC13	YC15	YC16	YC17	YC19	YC27	YC32
LREE	43.85	142.8	20.76	26.30	154.9	17.03	25.31	29.17	20.67	14.20	35.28	13.99	116.4	96.3
HREE	6.15	18.25	2.52	2.99	15.48	3.5	4.66	6.76	4.00	2.30	5.27	2.70	16.08	14.76
LREE/HREE	7.13	7.82	8.25	8.80	10.01	4.86	5.43	4.31	5.16	6.16	6.70	5.19	7.24	6.52
$(La/Yb)_N$	7.83	8.77	8.63	9.49	10.89	3.93	4.87	3.95	5.09	6.00	6.18	5.34	8.91	7.58
La/Sc	3.15	1.74	8.22	8.02	1.71	2.20	3.66	3.67	1.63	2.06	1.91	2.4	2.1	2.10
La/Th	5.12	2.56	3.30	3.82	3.38	2.10	2.08	3.84	2.84	1.92	2.81	2.09	3.24	3.79
Co/Th	0.7	1.57	0.3	0.3	3.7	0.62	1.00	0.7	1.2	0.19	0.54	0.3	1.30	1.36
δU	0.98	0.78	0.71	0.71	0.99	0.99	0.98	0.99	0.98	0.99	0.99	0.98	0.55	0.6
V/Cr	1.80	1.24	1.0	1.35	1.70	0.99	1.64	1.65	1.31	1.30	0.58	0.3	1.49	0.9
Ni/Co	4.40	2.48	4.12	4.14	2.51	4.25	0.9	2.22	3.16	3.41	5.25	17.9	3.1	1.68
Sr/Ba	1.41	0.58	0.31	0.32	3.02	1.17	1.38	0.86	1.45	0.91	1.55	1.39	0.46	0.37
Sr/Cu	135.6	6.03	61.14	61.85	28.10	177.1	59.35	109.7	84.0	65.15	81.64	85.87	7.27	9.55

[a]N is standard for chondrite. LREE = La + Ce + Pr + Nd + Sm + Eu, HREE = Gd + Tb + Dy + Ho + Er + Tm + Yb + Lu. δU = U/(0.5*(Th/3 + U)).[38]

content ranges between 1.86% and 3.51%, with an average of 2.74%. The CaO content varies from 3.32% to 9.08%, with an average of 6.08%, and the TiO_2 content ranges from 19.02% to 27.23%, with an average of 23.38%.

Based on the morphology, distribution, and associated mineral assemblages, uranium minerals in the Shawan Formation exhibit the following three modes of occurrence:

(1) Uranium minerals are primarily found between clastic particles, mainly as pitchblende and coffinite. Pitchblende grains are smaller, around 5 μm, appearing as irregular granular particles located within quartz fissures (Figure 6a) or apatite pits (Figure 6b), and are commonly associated with zircon (Figure 6c). Coffinite grains range from 5 to 60 μm in size, forming irregular clumps or granular aggregates that dissolve albite (Figure 6d), and are distributed along the edges, cracks, or pits of clastic albite (Figure 6e).

(2) Uranium minerals, predominantly coffinite, coexist with pyrite. Coffinite appears as colloidal around framboidal pyrite (Figure 6f) or as irregular masses at the edges of framboidal pyrite (Figure 6g).

(3) Uranium minerals, mainly coffinite, are found within calcite cements. Coffinite occurs as banded, dispersed grains (Figure 6h), or microgranular aggregates filling calcite dissolution pits (Figure 6i). Titanium−uranium oxides are irregularly distributed between sparry calcite (Figure 6j).

5. DISCUSSION

5.1. Rock Types and Provenance. The composition of sandstone is directly influenced by the properties of the source rock, which undergoes a series of processes including erosion, weathering, transportation, deposition, and diagenesis, all of which can significantly affect the sandstone's composition. The Chemical Index of Alteration (CIA) is an effective metric for reflecting the degree of weathering of the source rock.[40] A higher CIA value indicates a higher degree of chemical weathering, with values between 50%−70% representing weak weathering, 70%−80% indicating intermediate weathering, and values greater than 80% suggesting strong weathering. The A-CN-K triangulation which can represent the CIA value.[34,39] The three end elements are Al_2O_3, CaO* + Na_2O and K_2O. The CIA index ranges from 54% to 73.35% (with an average of 60.68%), which is significantly higher than the upper crust average of 49.21%, indicating weak weathering (Figure 7a). Additionally, the index of compositional variability (ICV) is often used to evaluate the degree of change in the original composition of clastic rocks, helping to determine whether the clastic rocks represent first-cycle sediments or are derived from recycled sediments or those that have undergone strong weathering.[35] The ICV value ranges from 0.59 to 5.88 with an average of 3.3. Except for some black oil-immersed sandstone and grayish-green mudstone, the ICV values of mineralized sandstone and oxidized sandstone are all greater than 1. It shows that the composition of sandstone is low, and it is the first deposit in the tectonic belt, and it has not experienced the process of sedimentary recycling.

Major elements can be used to determine the classification and compositional maturity of sedimentary rocks. The sandstone types in the Shawan Formation include lithic sandstone, subarkose and greywacke (Figure 7b). The discrimination diagrams (F1−F2, F3−F4) for source rock

https://doi.org/10.1021/acsomega.4c07825
ACS Omega 2024, 9, 48681−48696

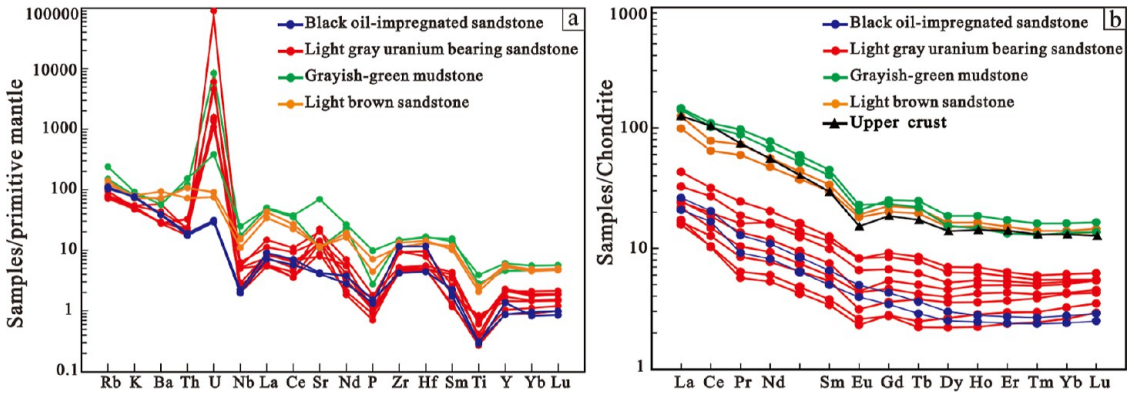

Figure 5. Chondrite and primitive mantle normalized spider diagrams for sandstone and mudstone of the Shawan Formation. (a) Primitive mantle-normalized trace element distribution curves. (b) Chondrite-normalized rare earth element distribution curves. Chondrite and primitive mantle-normalized data are taken from Sun and McDonough.[37]

Table 3. EPMA Results of Uranium Minerals in Sandstone of Shawan Formation (Composition in %; bdl, Below Detection Limit)

no.	SiO_2	Al_2O_3	MgO	CaO	Na_2O	TiO_2	FeO	Y_2O_3	P_2O_5	UO_2	PbO	ThO_2	MoO_3	MnO	total	type
1	7.65	1.65	0.40	3.29	1.00	2.92	0.82	0.15	1.09	62.44	bdl	bdl	1.92	0.49	83.82	coffinite
2	6.72	1.90	0.34	3.09	1.13	3.11	0.60	bdl	1.22	65.11	bdl	bdl	2.68	0.43	86.33	coffinite
3	6.33	1.77	0.24	3.51	0.63	2.47	0.70	0.05	0.99	64.99	bdl	bdl	2.42	0.43	84.53	coffinite
4	11.48	1.69	0.27	2.81	0.65	2.42	0.68	0.10	1.01	62.50	bdl	bdl	2.63	0.22	86.46	coffinite
5	9.45	3.37	0.37	5.72	0.72	3.10	0.67	bdl	0.79	62.57	bdl	bdl	2.78	0.51	90.05	coffinite
6	11.78	4.41	0.35	3.26	0.54	3.32	0.78	0.08	1.14	57.18	bdl	bdl	3.27	0.35	86.46	coffinite
7	10.88	1.95	0.28	4.22	1.03	2.37	0.81	0.02	1.09	62.35	bdl	bdl	2.91	0.48	88.39	coffinite
8	8.50	2.68	0.55	4.81	1.16	2.32	0.98	bdl	1.11	59.51	bdl	bdl	1.49	0.55	83.66	coffinite
9	6.96	1.96	0.39	6.51	0.91	2.82	1.00	0.02	1.14	64.15	bdl	bdl	2.56	0.51	88.93	coffinite
10	6.18	1.84	0.36	5.86	0.96	2.18	0.94	0.04	0.82	65.14	bdl	bdl	1.11	0.74	86.17	coffinite
11	7.47	2.31	0.42	1.91	0.78	2.30	0.77	0.13	0.90	61.42	bdl	bdl	1.24	0.26	79.91	coffinite
12	10.00	2.75	0.20	2.88	2.51	3.36	0.45	bdl	0.87	59.62	bdl	bdl	1.73	0.35	84.72	coffinite
13	12.59	3.99	0.50	5.86	0.71	2.54	0.79	bdl	0.68	55.23	bdl	bdl	2.75	0.57	86.21	coffinite
14	9.28	1.80	0.39	7.64	1.02	2.31	1.30	bdl	0.85	65.27	bdl	bdl	2.08	1.11	93.05	coffinite
15	8.00	2.18	0.31	7.68	0.98	2.24	0.50	0.11	0.86	59.71	bdl	bdl	3.48	0.83	86.88	coffinite
16	0.92	0.02	0.03	3.74	0.05	bdl	0.54	0.08	2.82	85.29	1.94	1.28	0.09	0.57	97.37	pitchblende
17	1.31	0.06	0.03	4.92	0.05	bdl	0.60	0.22	5.48	82.90	1.84	0.91	0.01	0.67	99.00	pitchblende
18	0.61	bdl	bdl	bdl	0.25	bdl	bdl	2.27	0.01	80.62	2.47	2.86	bdl	bdl	89.09	pitchblende
19	1.61	bdl	bdl	0.03	0.13	bdl	bdl	1.47	0.05	80.88	2.43	3.76	bdl	bdl	90.36	pitchblende
20	1.01	bdl	bdl	0.14	0.17	bdl	0.01	1.17	0.10	85.49	1.50	1.88	bdl	0.03	91.5	pitchblende
21	3.32	1.63	0.31	3.32	1.05	27.23	3.12	bdl	1.04	43.44	bdl	bdl	6.18	0.64	91.28	titanium−uranium oxide
22	2.50	0.84	0.21	5.28	0.85	26.07	0.65	bdl	1.00	56.20	bdl	bdl	2.18	0.52	96.3	titanium−uranium oxide
23	3.51	1.29	0.19	6.45	1.05	19.02	1.76	0.04	0.94	51.52	bdl	bdl	7.70	0.75	94.22	titanium−uranium oxide
24	1.86	0.34	0.13	9.08	0.80	21.73	0.41	bdl	1.22	55.27	0.01	bdl	1.06	0.67	92.58	titanium−uranium oxide
25	2.51	0.79	0.16	6.29	0.97	22.86	0.48	0.12	1.22	58.72	bdl	bdl	1.07	0.58	95.77	titanium−uranium oxide

types can effectively differentiate provenance areas.[34] Most samples fall within the fields of felsic igneous rock sources and near the intersection with intermediate igneous rock sources, with a few samples falling within the quartzose sedimentary provenance region (Figure 7c,d). Trace elements (such as Th, Sc, La, and Co) and their ratios also provide valuable indicators of the provenance of clastic rocks. The La/Th−Hf diagram shows that the samples are located within the felsic island arc source region (Figure 7e).[41] The Co/Th−La/Sc diagram indicates that the source rocks for the Shawan Formation are primarily felsic volcanic rocks, with some samples falling near the granitic and andesitic fields (Figure 7f).[42] Combined with the geological context, the sandstones of the Shawan Formation are primarily composed of felsic material with a minor intermediate component.

5.2. Tectonic Environment. Inert trace elements such as La, Th, Zr, and Sc are minimally affected by weathering and diagenetic processes, making them useful indicators of the tectonic background and evolutionary patterns of the source area.[36,45] The samples are primarily located in the continental island arc region (Figure 8), indicating that the tectonic setting of the Shawan Formation is primarily dominated by a continental island arc environment.

Located in the southern part of the Paleo-Asian Ocean tectonic domain, the Junggar Basin is an essential component of the Central Asian Orogenic Belt. The Carboniferous-Permian period was the main orogenic and basin-forming stages of the basin.[46,47] Since the Jurassic, the Zaire Mountain in the northern Chepaizi Uplift has gradually risen, forming a belt of Carboniferous to Permian intermediate-acidic volcanic clastic rocks. South of the Chepaizi Uplift, the North Tianshan

https://doi.org/10.1021/acsomega.4c07825
ACS Omega 2024, 9, 48681−48696

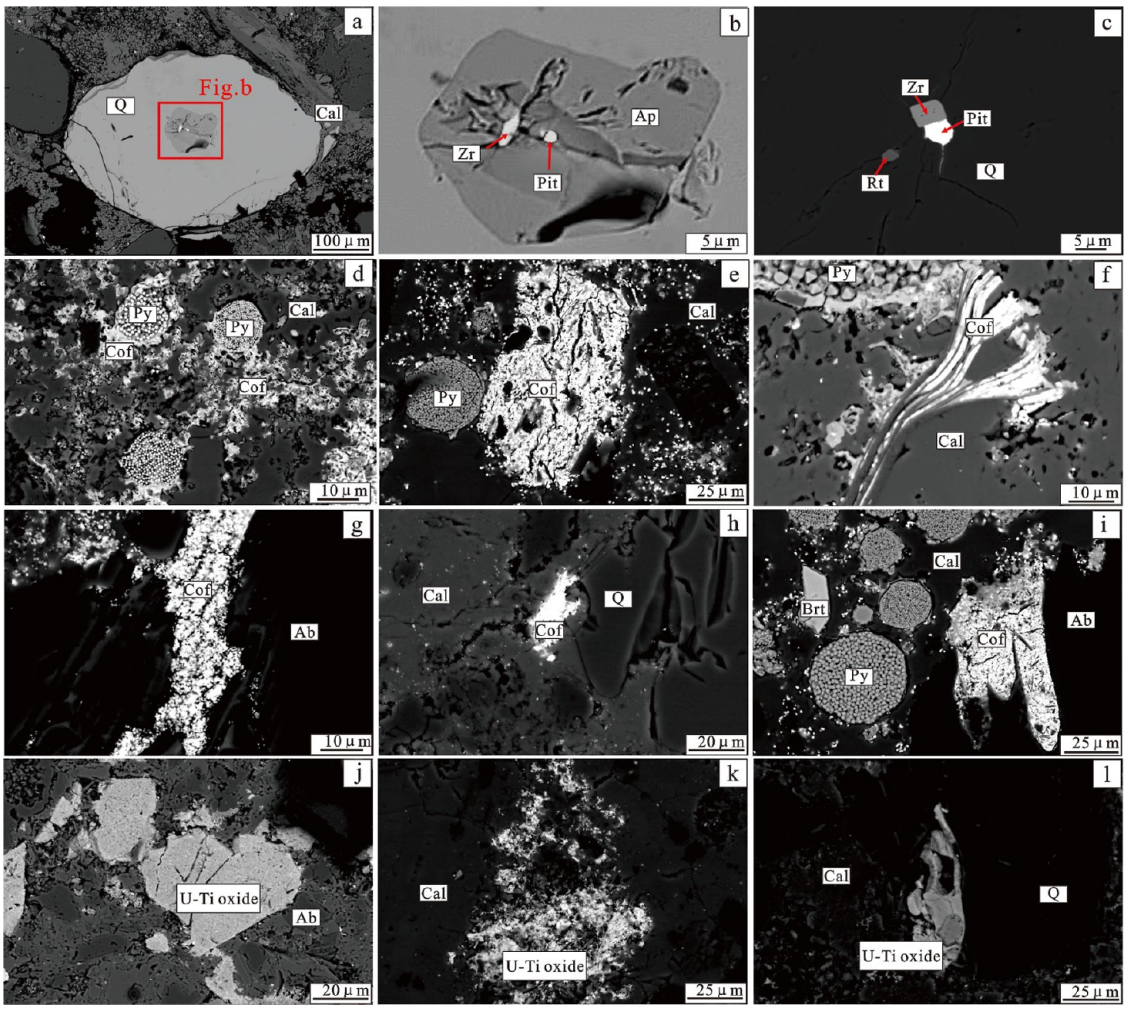

Figure 6. Back scattering image of uranium minerals in Shawan Formation. (a) Short columnar pitchblende. (b) Pitchblende in apatite pits. (c) Pitchblende in contact with zircon, distributed in quartz fractures. (d) Collophane coffinite encapsulating framboidal pyrite. (e) Coffinite aggregates distributed along the edges of framboidal pyrite. (f) Banded coffinite in calcite fractures. (g) Coffinite aggregates corroding albite. (h) Massive coffinite in calcite dissolution cavities. (i) Coffinite corroding albite. (j) Titanium−uranium oxides in calcite dissolution cavities. (k) Disseminated titanium−uranium oxides in calcite microfractures. (l) Massive titanium−uranium oxides corroding quartz. Pit: Pitchblende; Cof: Coffinite; Ti−U oxide: Titanium−uranium oxide; Py: Pyrite; Cal: Calcite; Q: Quartz; Zr: Zircon; Rt: Rutile; Ap. Apatite; Ab: Albite; Kfs: K-feldspar.

has experienced intense thrusting since the Mesozoic, leading to the development of an ophiolitic mélange belt.[48]

Previous studies have determined the age of the granodiorite porphyry in the Baogutu area on the southern margin of Zaire Mountain to be 310−319 Ma.[50,51] The age of the alkaline granite exposed in the Miaoergou pluton is 309 ± 1.4 Ma.[52−54] The age of the alkaline granite in the Akebasitao pluton is 303 ± 3 Ma, while the age of the Karamay pluton alkaline granite is 313.2 ± 2.5 Ma.[55] In the Sikeshu Depression, located in the southern part of the Chepaizi Uplift, a large number of Carboniferous-Permian intrusive rocks are exposed.[56] The lithology and formation ages are as follows: quartz diorite (324.1 ± 4.3 Ma), monzogranite (314.9 ± 4.1 Ma), and potassic granite (311.5 ± 3.9 Ma).[57] Combining this with the zircon age of approximately 344 ± 3.4 Ma from the Bayingou diabase, it is preliminarily concluded that the formation age of the North Tianshan suture zone is about 311.5−344 Ma,[49] with the main collisional orogeny occurring between 311 and 324 Ma.[56] The detrital zircon U−Pb age peaks in the sandstone of the first member of the Shawan Formation ($N_1s_1^1$) in the Chepaizi Uplift are 312 and 336 Ma.[57] This corresponds to the major magmatic activity in the Zaire Mountain on the northwest margin of the Chepaizi Uplift, indicating that the source supply direction was primarily from the northwest, i.e., the Zaire mountain. The U−Pb ages of detrital zircons in the sandstone of the second member of the Shawan Formation ($N_1s_1^2$) exhibit multiple peaks, with the primary peak at 374 Ma and secondary peaks at 293 and 403 Ma.[57] The zircon ages of the second member of the Shawan Formation ($N_1s_1^2$) also show multiple peaks, reflecting a source superposition area with contributions primarily from the northwest Zaire Mountain and the southern North Tianshan. Due to the remote impact of the collision between the Indian Plate and the Eurasian Plate, the Tianshan experienced intense compression and uplift, leading to the formation of a strongly asymmetrical sedimentary pattern within the Junggar Basin, which provided abundant clastic sediments to the Chepaizi Uplift. The observation of numerous granite fragments (Figure 3f) and rhyolite fragments (Figure 3g) under the microscope further provides necessary supporting evidence for the above viewpoint.

https://doi.org/10.1021/acsomega.4c07825
ACS Omega 2024, 9, 48681−48696

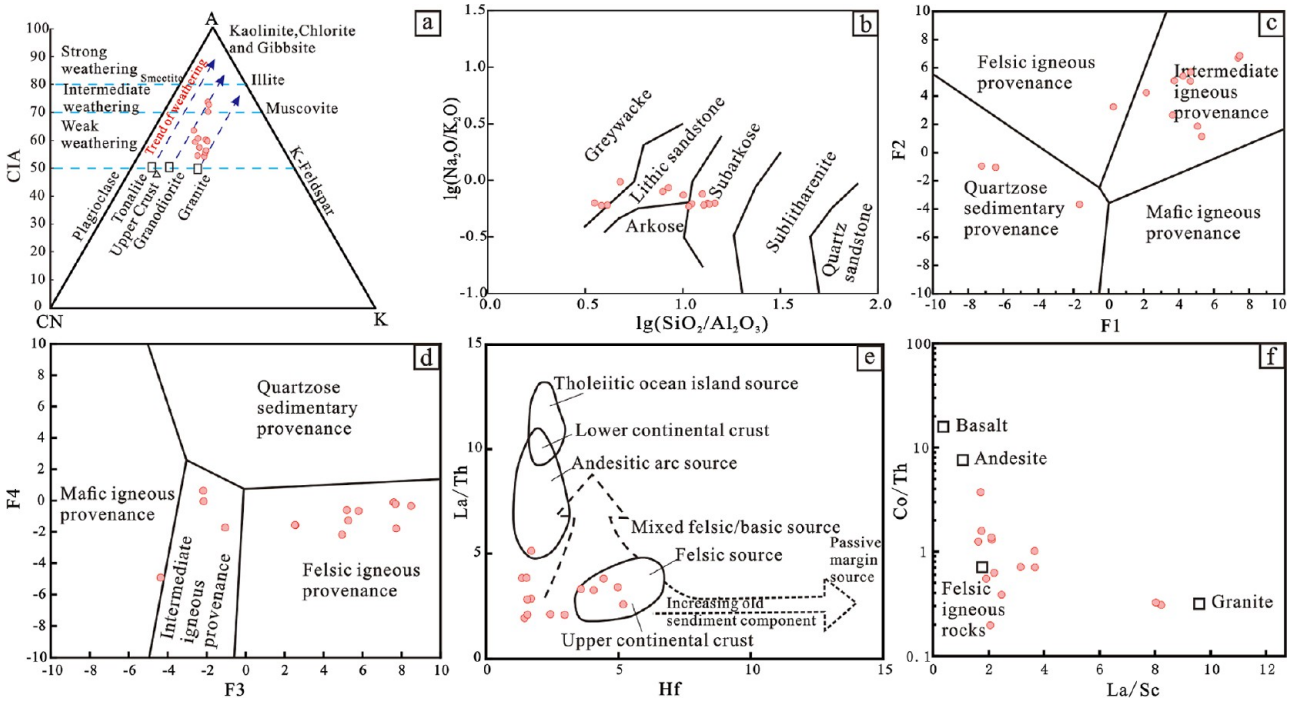

Figure 7. Discrimination diagrams for weathering intensity and provenance characteristics of the Shawan Formation. (a) A-CN-K diagram of sandstone (Revised from Nesbitt and Young[43]). (b) Major element discrimination diagram for sandstone types (Revised from Pettijohn et al.[44]). (c) F1−F2 discrimination diagram for sandstone provenance (Revised from Roser and Korsch[34]). (d) F3−F4 discrimination diagram for sandstone provenance (Revised from Roser and Korsch[34]). (e) Hf−La/Th discrimination diagram for sandstone provenance (Revised from Floyd and Leveridge[41]). (f) Co/Th−La/Sc source rock discrimination diagram (Revised from Gu et al.[42]). (a) Adapted with permission from ref 43. Copyright: [Geochimica et Cosmochimica Acta, 1984]. (b) Adapted from ref 44 Copyright: [New York: Springer-Verlag, 1972]. (c,d) Adapted from ref 34 Copyright: [Chemical Geology, 1988]. (e) Adapted from ref 41 Copyright: [Journal of the Geological Society, 1987]. (f) Adapted from ref 42 Copyright: [International Sedimentological Researches, 2002].

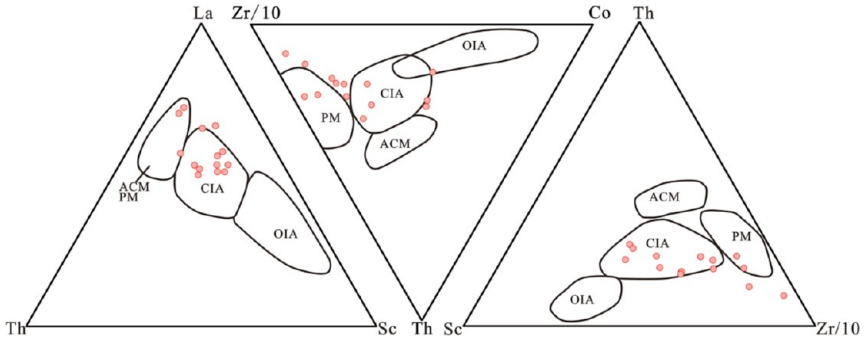

Figure 8. Discrimination diagram of trace elements for tectonic background of the Shawan Formation (Revised from Bhatia and Crook[58]). ACM: active continental margin. OIA: oceanic island arc. CIA: continental island arc. PM: passive continental margin. Adapted from ref 58 Copyright: [Contributions to Mineralogy and Petrology, 1986].

5.3. Reconstruction of Sedimentary Environment. The trace element properties in clastic sedimentary rocks are influenced by the nature of the source area's parent rocks and the tectonic setting.[59−63] Ratios of environmentally sensitive trace elements can reflect changes in depositional environments, such as paleo-oxidation−reduction conditions, paleosalinity, and paleoclimate (Table 4). The V/(V + Ni) ratio in the sandstone of the Shawan Formation ranges from 0.42 to 0.91, with an average of 0.71, indicating moderate water stratification, smooth circulation, and a suboxic aquatic environment. The V/Cr ratio ranges from 0.3 to 1.8, with an average of 1.24, suggesting oxidizing environment. The δU ratio ranges from 0.55 to 0.99, with an average of 0.87, also indicating oxidizing environment. The Sr/Ba ratio ranges from 0.31 to 3.02, with an average of 1.08, indicating a continental brackish water environment with relatively high salinity. The Sr/Cu ratio ranges from 6.03 to 177.1, with an average of 69.47, suggesting a dry and hot paleoclimate.[64]

The CIA and ICV indices reveal a distinct vertical trend: CIA values initially decrease before rising, while ICV values increase, followed by a sudden drop. This pattern reflects fluctuations in the weathering intensity of source rocks, shifting from strong to weak and back to strong, suggesting the influence of thermal events in the source area since the Neogene. Basin evaporation was significant, and water salinity was relatively high. The paleoenvironment likely featured an arid, continental, semisaline water setting with paleoredox conditions indicative of a weakly oxidizing, hot, and dry

https://doi.org/10.1021/acsomega.4c07825
ACS Omega 2024, 9, 48681−48696

Table 4. Geochemical Paleoclimate Environment Reconstruction Discriminant Index

		palaeoredox condition			
Discrimination parameters	sample data/average values in this study	anoxic environment		oxidizing environment	reference
		anaerobic environment	hypoxic environment		
V/(V + Ni)	0.42−0.91/0.71	0.4−0.6	0.6−0.84	>0.84	Hatch and Leventhal[65]
V/Cr	0.3−1.8/1.24	>4.25	2−4.25	<2.0	Tribovillard et al.[66]
δU	0.55−0.99/0.87	>1.0		<1.0	Lecomte et al.[38]
		paleosalinty condition			
discrimination parameters	sample data/average values in this study	marine seawater	terrestrial freshwater		reference
			brackish water environment	microhaline environment	
Sr/Ba	0.31−3.02/1.08	>1.0	0.6−1.0	<0.6	Wang et al.[67]
		paleoclimatic condition			
discrimination parameters	sample data/average values in this study	arid and hot climate	tropical and humid climate		reference
Sr/Cu	6.03−177.1/69.47	>5.0	<5.0		Lerman[68]

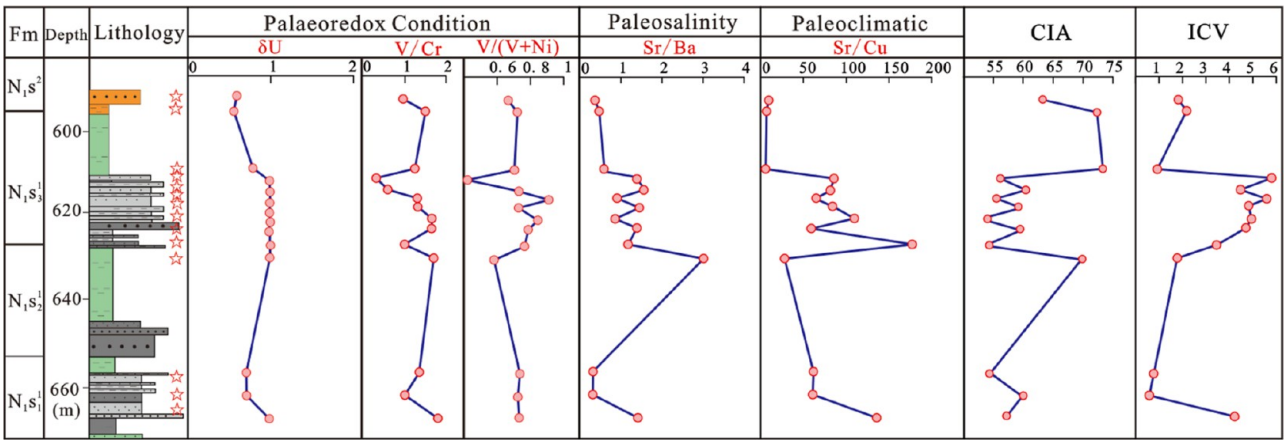

Figure 9. Sedimentary environment evolution of the Shawan Formation.

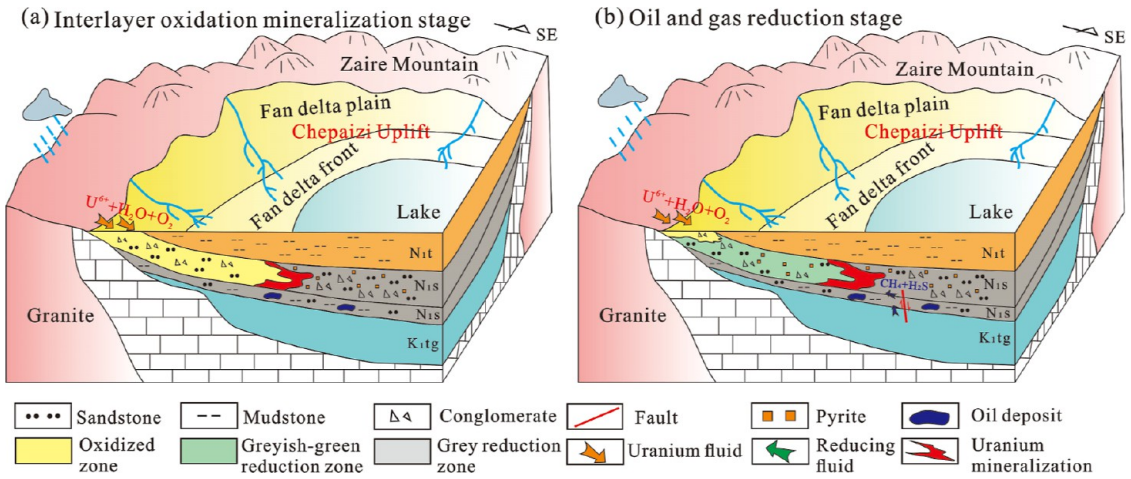

Figure 10. Uranium mineralization model of the Shawan Formation in the Chepaizi Uplift, Junggar Basin. (Revised from Liu et al.[75]). Adapted with permission from ref 75. Copyright: [Minerals, 2022].

climate (Figure 9). While such an environment is conducive to the migration of uranium, it is not favorable for the preservation of uranium deposits. However, current findings reveal that the uranium-bearing layers are all located in the upper parts of the oil-bearing strata, where oil stains and traces are visible in the mineralized sandstone bodies. Under the microscope, sparry calcite also shows signs of hydrocarbon fluorescence. It is preliminarily speculated that hydrocarbon leakage provided an external reducing agent for the uranium mineralization in the Shawan Formation.

5.4. Discussion on Uranium Mineralization. The Carboniferous magmatic rocks in the eroded margin area of the northwestern Chepaizi Uplift, particularly in the Zaire Mountain region, are highly developed and mainly consist of

https://doi.org/10.1021/acsomega.4c07825
ACS Omega 2024, 9, 48681−48696

intermediate to acidic magmatic rocks.[69] Notably, the biotite potassium granite in the Miaoergou area of Zaire Mountain contains uranium concentrations ranging from 0.64×10^{-6} to 3.28×10^{-6}, with an average of 1.7×10^{-6}; thorium concentrations range from 3.65×10^{-6} to 12.04×10^{-6}, with an average of 8.25×10^{-6}. The Th/U ratio is between 2.24 and 10.0, with an average of 5.15.[26] The leaching rate of active uranium is 1.64% to 3.59%, with an average of 2.62%, the highest among the periphery of the Junggar Basin.[70,71] This indicates that these plutons have provided a uranium source to the interior of the Chepaizi Uplift after diagenesis. The porosity of the sandstone in the Shawan Formation ranges from 22.9% to 39.7%, with an average of 33.66%, and permeability ranges from $(54.1-9490) \times 10^{-3}$ μm^2, with an average of 3436.8×10^{-3} μm^2.[28] This reflects the high porosity and good permeability of the sandstone, which can serve as effective conduits for the migration of uranium-bearing fluids. Influenced by the regional Darbut Fault in the northwest, the uranium-rich granites in Zaire Mountain have undergone intense destruction, leading to well-developed structural fissure water systems. Atmospheric precipitation and glacier meltwater favor the recharge of the Neogene aquifer groundwater, while uranium- and oxygen-bearing water flows or is artesian along the slope of the Shawan Formation, facilitating the infiltration and migration of oxygenated groundwater carrying active uranium through the sandstone bodies of the Shawan Formation. During the early Neogene, the climate was humid, shifting to semiarid conditions in the Pliocene, and becoming arid in the Pleistocene and Holocene, characterized by alternating wet and dry periods.[72] The uplift of the crust during the Quaternary Himalayan orogeny led to a drop in groundwater levels and intensified groundwater circulation. The oxidation zone extends deeply along sandstone layers, promoting the activation and migration of uranium, increasing its concentration in water, and resulting in pre-enriched within the redox transition zone (Figure 10a).

Additionally, the Chepaizi Uplift is located adjacent to hydrocarbon-generating depressions. In the Shawan depression to the east, high-maturity, organic-rich lacustrine source rocks of the Middle Permian Wuerhe Formation have developed.[73] To the south, the Sikeshu depression features a coal-bearing lacustrine and swamp facies sequence from the Lower Jurassic Badaowan Formation, which has reached the hydrocarbon generation threshold.[74] Tectonic movements have induced the formation of intralayer fractures, enabling deep-seated cracked gas from oil and associated gases to migrate upward along faults and fractures into the more porous sandstone layers of the Shawan Formation, making the Chepaizi Uplift a favorable reception area for long-term hydrocarbon migration. The hydrocarbons and their derivative reducing agents, such as H_2S and CH_4, reduce Fe^{3+} in the sandstone to Fe^{2+}. This reduction transforms the originally yellow sandstone, formed under oxidizing conditions, into grayish-green sandstone under weakly reducing conditions, creating potential ore-hosting strata. The highly reducing hydrocarbon fluids reduce activated U^{6+} uranyl compounds to stable U^{4+} coffinite, leading to the precipitation and enrichment of uranium at the interface between the gray and grayish-green sandstone bodies (Figure 10b). Moreover, the hydrocarbon fluids can establish a strong reductive geochemical barrier, which is conducive to the preservation of uranium deposits in later stages.

6. CONCLUSION

(1) The main types of uranium minerals in the Shawan Formation are coffinite, followed by titanium−uranium oxides and minor amounts of pitchblende. Coffinite, is found in three distinct forms: as colloidal inclusions enveloping framboidal pyrite, as short prismatic aggregates eroding albite, and as banded or irregular masses distributed among calcite cement.

(2) The elemental ratios such as δU, V/Cr, V/(V + Ni), Sr/Ba, and Sr/Cu indicate that the Shawan Formation was influenced by Neogene thermal events, with significant evaporative processes in the basin. The water salinity was relatively high, and the ancient water medium was characterized as an arid continental semisaline environment. The overall paleoredox conditions were indicative of a weakly oxidizing dry and hot environment.

(3) Uranium mineralization occurs in two stages. In the early stage, uranium-containing oxygenated water migrated laterally along slope zones, where uranium became pre-enriched in the redox transition zone. In the later stage, hydrocarbons ascended along unconformities and fault structures, leading to the secondary reduction of the interlayer oxidation zone in the Shawan Formation, resulting in uranium mineralization and enrichment at the interface between gray and grayish-green sandstone bodies.

■ ASSOCIATED CONTENT

Data Availability Statement

The original contributions presented in the study are included in the article, further inquiries can be directed to the corresponding author.

■ AUTHOR INFORMATION

Corresponding Author

Mangen Li − *School of Earth Sciences, East China University of Technology, Nanchang, Jiangxi Province 330013, China; National Key Laboratory of Uranium Resource Exploration-Mining and Nuclear Remote Sensing, Nanchang 330013 Jiangxi Province, China*; Email: mgli@ecut.edu.cn

Authors

Niannan Chen − *School of Earth Sciences, East China University of Technology, Nanchang, Jiangxi Province 330013, China; State Key Laboratory of Nuclear Resources and Environment, East China University of Technology, Nanchang, Jiangxi Province 330013, China*; orcid.org/0009-0004-8699-0064

Guangzhen Mao − *Geological Party No. 216, China National Nuclear Corporation, Urumqi 830011 Xinjiang Autonomous Region, China*

Xiangfei Tang − *Geological Party No. 216, China National Nuclear Corporation, Urumqi 830011 Xinjiang Autonomous Region, China*

Shengming Wu − *Geological Party No. 216, China National Nuclear Corporation, Urumqi 830011 Xinjiang Autonomous Region, China*

Jianbing Duan − *School of Earth Sciences, East China University of Technology, Nanchang, Jiangxi Province 330013, China; State Key Laboratory of Nuclear Resources and Environment, East China University of Technology, Nanchang, Jiangxi Province 330013, China*

https://doi.org/10.1021/acsomega.4c07825
ACS Omega 2024, 9, 48681−48696

Baowen Guan − *School of Earth Sciences, East China University of Technology, Nanchang, Jiangxi Province 330013, China; State Key Laboratory of Nuclear Resources and Environment, East China University of Technology, Nanchang, Jiangxi Province 330013, China*

Pengfei Fan − *School of Earth Sciences, East China University of Technology, Nanchang, Jiangxi Province 330013, China; State Key Laboratory of Nuclear Resources and Environment, East China University of Technology, Nanchang, Jiangxi Province 330013, China;* orcid.org/0009-0005-8528-9804

Rui Jin − *School of Earth Sciences, East China University of Technology, Nanchang, Jiangxi Province 330013, China*

Jin Wang − *School of Earth Sciences, East China University of Technology, Nanchang, Jiangxi Province 330013, China*

Complete contact information is available at: https://pubs.acs.org/10.1021/acsomega.4c07825

Funding

Geological Party No. 216, China National Nuclear Corporation project-Study on the Sedimentary Environment of Late Cretaceous-Miocene in the Central Junggar Basin, Xinjiang (Project Number: H202200098); East China University of Technology, Graduate Innovation Fund—Tectonic evolution of the eastern Junggar Basin and its control on sandstone-type uranium mineralization (Project Number: YC2023-S575); Joint Innovation Fund Project between the State Key Laboratory of Nuclear Resources and Environment, East China University of Technology, and China Uranium Corporation-A detailed study on the sedimentary characteristics of the Saihan Formation, a key ore-bearing stratum of sandstone uranium deposits in the Erlian Basin (Project Number: 2022NRE-LH-12); Development Fund Project of State Key Laboratory of Nuclear Resources and Environment-Mesozoic uplifting of Bogda Mountain and its control of uranium mineralization enrichment in Tuha and Junggar basins (Project Number: 2020NRE14); Science and Technology Research Project of Jiangxi Provincial Department of Education—The implication of the uplift-exhumation of the Bogda Mountains of the Mesozoic constrained by zircon and apatite fission track thermochronology (Project Number: GJJ2200710); East China University of Technology PhD Project—Genetic research of Daqing Manganese Deposit in Southeast Yunnan Province (Project Number: DHBK2018034); East China University of Technology, Graduate Innovation Fund—Mineralogical Characteristics and Metallogenic Mechanism of Neogene sandstone Type Uranium Deposit in Chepaizi Uplift, west margin of Junggar Basin, China (Project Number: YC2024-B204).

Notes

The authors declare no competing financial interest.

■ ACKNOWLEDGMENTS

We sincerely appreciate the assistance provided by no. 216 Geologic Party of China National Nuclear Corporation in field work. Special thanks to the anonymous reviewers for their comments and suggestions.

■ REFERENCES

(1) Zhang, J. D. Innovation and development of the ore-forming theory of sandstone-type uranium deposits in China. *Uranium Geol.* **2016**, *32* (06), 321−332.

(2) Jin, R. S.; Teng, X. M. Large-scale mineralization of sandstone-type uranium deposits in northern China. *North China Geol.* **2022**, *45* (1), 42−57.

(3) Zhang, P. F.; Li, F. J.; Liu, Y. X.; Liu, Z. L.; Peng, N.; Ma, X. K.; Liu, B.; Ogg, J. G. Mesozoic-cenozoic exhumation history and its implications for uranium mineralization in the southern Junggar Basin, North China. *Ore Geol. Rev.* **2022**, *144*, 104784.

(4) Zhong, L.; Nie, F. J.; Wang, G. The relationship between the characteristics of sandbody and uranium mineralization of Toutunhe Formation of the Middle Jurassic in Kamster area, eastern margin of Junggar Basin. *Sci. Technol. Eng.* **2019**, *19* (26), 75−82.

(5) Sun, X.; Wang, G. R.; Wang, G.; Lu, K. G. Analysis of paleoclimate and environment from the Middle Jurassic to Eocene in the eastern Kamster area and its influence on sandstone-type uranium deposits. *Xinjiang Geol.* **2019**, *37* (02), 242−246.

(6) Lian, G.; Tang, X. F.; Huang, S. Geochemical characteristics and geological significance of lower sandstone of Toutunhe Formation in the eastern Kamster area of the Junggar Basin. *Uranium Geol.* **2023**, *39* (04), 546−557.

(7) Wu, Z. J.; Han, X. J.; Ji, H.; Cai, Y. F.; Xue, L.; Sun, S. J. Mesozoic-cenozoic tectonic events of eastern Junggar Basin, NW China and their significance for uranium mineralization: insights from seismic profiling and AFT dating analysis. *Ore Geol. Rev.* **2021**, *139*, 104488.

(8) Hu, X. W.; Yang, X. Y.; Ren, Y. S.; Du, G. F.; Wu, Z. J. Genesis of interlayer oxidation zone-type uranium deposit in the channel conglomerates, Beisantai area, Junggar basin: an insight into uranium mineralization. *Ore Geol. Rev.* **2022**, *140*, 104557.

(9) Hu, X. W.; Yang, X. Y.; Wu, Z. J.; Ren, Y. S.; Miao, P. S. Sedimentological, petrological, and geochemical constraints on the formation of the Beisantai sandstone-type uranium deposit, Junggar Basin, NW China. *Ore Geol. Rev.* **2022**, *141*, 104668.

(10) Han, X. Z.; Wu, Z. J.; Lin, Z. X.; Wang, X. J.; Jiang, Z.; Ji, H.; Hu, H. Control of tectonic uplift and denudation on uranium mineralization in the eastern Junggar Basin. *J. China Coal Soc.* **2023**, *48* (9), 3471−3482.

(11) Mao, G. Z.; Tang, X. F.; Niu, J. J. Types and sources of crude oil in the Chepaizi uplift, northwest margin of the Junggar Basin. *Xinjiang Geol.* **2020**, *38* (1), 86−91.

(12) Pu, X. C.; Tang, X. F.; Zhang, Q.; Wu, S. M.; Niu, J. J.; Guo, C. Research and significance of Jurassic sandstone type U-mineralization at Jiangjun Gobi region in the east Junggar basin. *Contrib. Geol. Miner. Resour. Res.* **2022**, *37* (2), 199−206.

(13) Xin, X.; Xu, Q.; He, Z. B. Geochemical characteristics of Wulunguhe Formation oxidation zone and its relation to uranium mineralization in Dingshan area, Junggar Basin. *World Nucl. Geosci.* **2014**, *31* (1), 16−22.

(14) Zhang, J. J.; Mou, C. L.; He, M. Y.; Zhao, F. J.; Zhou, K. K.; Wu, H.; Chen, X. W.; Xia, Y. Geochemical characteristics and their geological significance of Wulunguhe Formation in Dingshan area, Junggar Basin. *Bull. Mineral Petrol. Geochem.* **2017**, *36* (6), 1026−1033.

(15) Chen, T.; Zhang, J. J.; Wang, S. C. Sedimentary environment and its effect on uranium mine of Wulunguhe Formation in Dingshan area, Junggar Basin. *Sci. Technol. Eng.* **2018**, *18* (20), 33−40.

(16) Wang, G. R.; Jia, W. W.; Du, M.; Huang, S.; Lu, K. G.; Sun, X. Relationship between Jurassic braided river depositional system and uranium mineralization in the southern margin of Junggar Basin. *Uranium Geol.* **2021**, *37* (03), 342−354.

(17) Jia, W. W.; Wang, G. R.; Tang, X. F.; Huang, S.; Yan, J. J. Discussion on the relationship of different types of alteration zones to the uranium mineralization in Toutunhe Formation of Louzhuangzi area, southern margin of Junggar Basin. *World Nucl. Geosci.* **2023**, *40* (02), 152−161.

(18) Lu, K. G.; Du, M.; Sun, X.; Jia, W. W.; Wang, S. Y. Metallogenic controlling factors and genetic analysis of sandstone uranium deposit in the lower member of Toutunhe Formation in Louzhuangzi area, southern Junggar Basin. *Uranium Geol.* **2023**, *39* (04), 507−521.

(19) Huang, S.; Jia, W. W.; Yan, J. J. Discussion on the relationship between sand body characteristics and uranium mineralization in the lower member of Toutunhe Formation in Louzhuangzi area, southern margin of Junggar Basin. *Uranium Geol.* **2023**, *39* (04), 522−532.
(20) Yu, Q. X.; Wang, J. Y.; Lu, Q. H.; Cao, Q. The distribution character and overlapping relationship between uranium and heavy crude oil in Chepaizi uplift of the Junggar Basin. *Pet. Geol. Exp.* **2010**, *32* (5), 428−433.
(21) Dang, L.; Tang, X. F. Prospects of neogene sandstone-type uranium mineralization in Chepaizi area, western Junggar Basin. *Mod. Min.* **2015**, *10*, 119−121.
(22) He, F.; He, S.; He, Z. B.; Jia, C.; Zhang, Z. L. Sedimentary characteristics and metallogenic prospect of sandstone type uranium deposit in Shawan Formation of Chepaizi uplift, Junggar Basin. *World Nucl. Geosci.* **2021**, *38* (4), 414−423.
(23) A, Z. M.; Fu, D. W.; Wang, G. R.; Du, M. Analysis on uranium mineralization controlling factors of the third sand layer in the first member of Shawan Formation in Chepaizi area, Junggar Basin. *Uranium Geol.* **2023**, *39* (01), 46−58.
(24) He, S.; Mao, G. Z.; Chen, H.; Wang, M. M. Struetural evolution and its control on uranium mineraization in Chepaizi uplift, westem Junggar basin, Xinjiang. *World Nucl. Geosci.* **2024**, *41* (4), 650−664.
(25) Hu, Z. W.; Mao, G. Z. Hydrogeological conditions of uranium mineralization of Chepaizi area in western Junggar Basin. *Uranium Min. Metall.* **2024**, *43* (02), 1−12.
(26) Zhao, L.; Hu, Z. G.; Huabei, M.; Mei, Z. H.; Qin, F.; Wu, C. W.; et al. Mineralization potential and prospecting direction of sandstone-type uranium deposits in the Chepaizi area in the western margin of Junggar Basin. *Geol. Prospect.* **2021**, *57* (3), 507−517.
(27) Mao, G. Z. Uranium mineralization characteristics, ore-controlling factors and prospecting direction of Neogene Shawan Formation in Chepaizi area, western Junggar Basin. *Uranium Geol.* **2023**, *39* (04), 569−580.
(28) He, D. F.; Zhang, L.; Wu, S. T.; Li, D.; Zhen, Y. Tectonic evolution stages and features of the Junggar Basin. *Petrol. Nat. Gas Geol.* **2018**, *39* (5), 845−861.
(29) Guo, Z. J.; Zhang, Z. C.; Wu, C. D.; Fang, S. H.; Zhang, R. The mesozoic and cenozoic exhumation history of Tianshan and comparative studies to the Junggar and Altai Mountains. *Acta Geol. Sin.* **2006**, *80* (01), 1−15.
(30) He, Z. B.; Liu, Z. Y.; Yang, Y.; Guo, Q.; Song, J. Y.; Ji, H. L. Mesozoic-cenozoic tectonic-sedimentary evolution and metallogenesis of sandstone-type uranium deposit in Junggar Basin. *Xinjiang Geol.* **2016**, *34* (3), 410−417.
(31) Qin, M. K.; He, Z. B.; Liu, Z. Y.; Guo, Q.; Song, J. Y.; Xu, Q. Study on metallogenic environments and prospective direction of sandstone-type uranium deposits in Junggar Basin. *Geol. Rev.* **2017**, *63* (5), 1255−1269.
(32) Hu, X. W.; Yang, X. Y.; Ren, Y. S.; Wu, Z. J.; Du, G. F.; Huang, T. T. Control of sedimentary environment-tectonic evolution on sandstone-type uranium mineralization in the Junggar Basin. *Geotect. Metallogenia* **2020**, *44* (04), 725−741.
(33) General Administration of Quality Supervision Inspection and Quarantine of the People's Republic of China. *Quantitative Analysis of Silicate Minerals by Electron Probe Method*. GB/T 15617-2002; Standards Press of China: Beijing, 2002.
(34) Roser, B. P.; Korsch, R. J. Provenance signatures of sandstone-mudstone suites determined using discriminant function analysis of major-element data. *Chem. Geol.* **1988**, *67* (1−2), 119−139.
(35) Cox, R.; Low, D. R.; Cullers, R. L. The influence of sediment recycling and basement composition on evolution of mudrock chemistry in the southwestern United States. *Geochim. Cosmochim. Acta* **1995**, *59*, 2919−2940.
(36) Taylor, S. R.; McLennan, S. M. *The Continental Crust: Its Composition and Evolution*; Blackwell Scientific Publications: Oxford, 1985; pp 1−312.
(37) Sun, S. S.; McDonough, W. F. Chemical and isotopic systematics of oceanic basalts: implications for mantle composition and processes. *Spec. Publ. Geol. Soc. Lond.* **1989**, *42* (1), 313−345.
(38) Lecomte, A.; Cathelineau, M.; Michels, R.; et al. Uranium mineralization in the Alum Shale Formation (Sweden): evolution of a U-rich marine black shale from sedimentation to metamorphism. *Ore Geol. Rev.* **2017**, *88*, 71−98.
(39) Rahman, M. A.; Das, S. C.; Pownceby, M. I.; Tardio, J.; Alam, M. S.; Zaman, M. N. Geochemistry of recent Brahmaputra river sediments: provenance, tectonics, source area weathering and depositional environment. *Minerals* **2020**, *10*, 813.
(40) Feng, L. J.; Chu, X. L.; Zhang, Q. R.; Zhang, T. G. Chemical index of alteration (CIA) and its applications in the neoproterozoic clastic rocks. *Earth Sci. Front.* **2003**, *10* (4), 539−544.
(41) Floyd, P. A.; Leveridge, B. E. Tectonic environment of the Devonian Gramscatho basin, south Cornwall: framework mode and geochemical evidence from turbiditic sandstones. *J. Geol. Soc.* **1987**, *144* (4), 531−542.
(42) Gu, X. X.; Liu, J. M.; Zheng, M. H.; Tang, J.; Qi, L. Provenance and tectonic setting of the proterozoic turbidites in Hunan, south China: geochemical evidence. *Int. Sediment. Res.* **2002**, *72*, 393−407.
(43) Nesbitt, H. W.; Young, G. M. Prediction of some weathering trends of plutonic and volcanic rocks based on thermodynamic and kinetic considerations. *Geochim. Cosmochim. Acta* **1984**, *48* (7), 1523−1534.
(44) Pettijohn, F. J.; Potter, P. E.; Siever, R. *Sand and Sandstone*; Springer-Verlag: New York, 1972; pp 1−553.
(45) Taylor, S. R.; McLennan, S. M. The geochemical evolution of the continental crust. *Rev. Geophys.* **1995**, *33* (2), 241−265.
(46) Huang, G. W.; Pan, J. Y.; Xia, F.; Yan, J.; Zhang, C. Y.; Wu, D. H.; Liu, Y. Provenance of uranium mineralization of the Yugia area, northwest china: constraints from detrital zircon U-Pb geochronology and Hf isotopes. *J. Earth Sci.* **2022**, *33* (6), 1549−1570.
(47) Zhang, Z. B.; Zhu, Z. J.; Li, H.; Jiang, W. C.; Wang, W. F.; Xu, Y.; Li, L. R. Provenance and salt structures of gypsum formations in Pb-Zn ore-bearing Lanping basin, Southwest China. *J. Cent. S. Univ.* **2020**, *27* (6), 1828−1845.
(48) Liang, Y. S. Geological structure and formation evolution of the Chepaizi uplift in the western Junggar Basin. Ph.D. Thesis, China University of Geosciences, Beijing, 2019.
(49) Xu, X. Y.; Li, X. M.; Ma, Z. P.; Xia, L. Q.; Xia, Z. C.; Peng, S. X. LA-ICP-MS zircon U-Pb dating of Gabbro from the Bayingou ophiolite in the Northern Tianshan mountains. *Acta Geol. Sin.* **2006**, *80* (8), 1168−1176.
(50) Wei, S. N.; Zhu, Y. F. Petrology, geochronology and geochemistry of intermediate-acidic intrusions in Baogutu area, West Junggar, Xinjiang. *Acta Petrol. Sin.* **2015**, *31* (1), 143−160.
(51) Hu, Y.; Wang, J. L.; Wang, J. Q.; Yang, M.; Yuan, P.; Ling, W. W. Geochemistry and geochronology of the Miaoergou granite pluton in West Junggar, Xinjiang. *Acta Petrol. Sin.* **2015**, *31* (2), 505−522.
(52) Huang, P. H.; Chen, X. H.; Wang, Z. H.; Ye, B. Y.; Li, X. Z.; Yang, Y. Late paleozoic granitic magmatism in West Junggar metallogenic belt, Xinjiang, Central Asia, and its tectonic implication. *Geotect. Metallogenia* **2016**, *40* (1), 145−160.
(53) FengHao, D.; Qian, Z.; YongJun, L.; Hong, X.; PanLong, W.; JiPeng, G. Petrogenesis and geodynamic setting of the late carboniferous granodiorite porphyry in Miaoergou pluton, southern West Junggar. *Acta Petrol. Sin.* **2021**, *37* (4), 1159−1176.
(54) Su, Y. P.; Tang, H. F.; Hou, G. S.; Liu, C. Q. Geochemistry of aluminous A-type granites along Darabut tectonic belt in West Junggar. *Xinjiang. Geochimica.* **2006**, *35* (1), 55−67.
(55) Ma, F. Z. Spatial-temporal distribution and petrogenesis of late paleozoic granitoids in the West Junggar. Doctoral Dissertation, Chinese Academy of Geological Sciences, 2020.
(56) Yang, G. H.; Zhang, W. B.; Guo, Y. F.; Fu, M. Q.; Si, G. H.; Su, H. P.; et al. LA-ICP-MS zircon U-Pb chronology and geological implications of Sikeshu stitching pluton in the North Tianshan Suture Zone, Xinjiang. *Northwest. Geol.* **2014**, *47* (2), 83−98.
(57) Li, Y.; Wu, C. D.; Zhang, X. C.; Xie, L. H.; Leng, J. X.; Guan, X. T. Heavy minerals characteristics, U-Pb geochronology and provenance analysis of Neogene Shawan formation in Chepaizi uplift, Junggar Basin. *J. Peking Univ.* **2021**, *57* (6), 1058−1070.

https://doi.org/10.1021/acsomega.4c07825
ACS Omega 2024, 9, 48681−48696

(58) Bhatia, M. R.; Crook, K. A. W. Trace element characteristics of graywackes and tectonic setting discrimination of sedimentary basins. *Contrib. Mineral. Petrol.* **1986**, *92* (2), 181−193.
(59) Zhang, Z. B.; Li, H.; Zheng, W.; Whattam, S. A.; Zhu, Z.; Jiang, W.; Zhao, D. Response of paleogene fine-grained clastic rock deposits in the South Qiangtang Basin to environments and thermal events on the Qinghai-Tibet Plateau. *ACS Omega* **2023**, *8* (29), 26458−26478.
(60) Sun, D.; Li, H. M.; Xia, F.; Nie, F.; Huang, G.; Zhang, Z.; Meng, F.; Pan, J.; Hu, Y. Provenance and tectonic setting of the lower cretaceous Huanhe formation in the Northwestern Ordos Basin and its implications for uranium mineralization. *ACS Omega* **2024**, *9* (3), 3324−3341.
(61) Zhang, Z. B.; Guo, Y. H.; Wei, H. Y.; Zeng, C. L.; Zhang, J. M.; Zhao, D. F. The intensification of prolonged cooling climate-exacerbated late ordovician−early silurian mass extinction: a case study from the Wufeng Formation−Longmaxi formation in the Sichuan Basin. *J. Mar. Sci. Eng.* **2023**, *11*, 1401.
(62) Meng, F.; Nie, F.; Xia, F.; Yan, Z.; Sun, D.; Zhou, W.; Zhang, X.; Wang, Q. Sedimentary environment, tectonic setting, and uranium mineralization implications of the Yimin formation, Kelulun depression, Hailar Basin, China. *J. Mar. Sci. Eng.* **2024**, *12*, 763.
(63) Meng, F.; Nie, F.; Xia, F.; Yan, Z.; Sun, D.; Zhou, W.; Zhang, X.; Wang, Q. Geochemical characteristics and detrital zircon U-Pb ages of the Yimin Formation, Kelulun Depression, Hailar Basin and constraints on uranium mineralization. *PLoS One* **2024**, *19* (8), No. e0309433.
(64) Harnois, L. The CIW index: a new chemical index of weathering. *Sediment. Geol.* **1988**, *55* (3−4), 319−322.
(65) Hatch, J. R.; Leventhal, J. S. Relationship between inferred redox potential of the depositional environment and geochemistry of the Upper Pennsylvanian (Missourian) Stark Shale Member of the Dennis Limestone, Wabaunsee County, Kansas, U.S.A. *Chem. Geol.* **1992**, *99* (1−3), 65−82.
(66) Tribovillard, N.; Algeo, T. J.; Lyons, T.; Riboulleau, A. Tracemetals as paleoredox and paleoproductivity proxies: an update. *Chem. Geol.* **2006**, *232* (1−2), 12−32.
(67) Wang, Y. Y.; Guo, W. Y.; Zhang, G. D. Application of some geochemical indicators in determining the sedimentary environment of the Funing Group (Paleogene), Jin-Hu depression, Jiangsu Province. *J. Tongji Univ.* **1979**, No. 2, 51−60.
(68) Lerman, A. *Lakes: Chemistry, Geology, Physics*; Springer-Verlag: Berlin, 1978; pp 79−83.
(69) Zhao, Z. H.; Bai, Z. H.; Xiong, X. L. *Alkaline-Rich Igneous Rocks and their Metallogenic Effects in Northern Xinjiang*; Geological Publishing House: Beijing, China, 2006; pp 1−308.
(70) Song, J. Y. Basement characteristics and sandstone-type uranium mineralization in the Junggar Basin. Doctoral Dissertation, Beijing Research Institute of Uranium Geology, 2014.
(71) Fan, P. F.; Li, M. G.; Huang, H. Y.; Huang, G. W.; Gu, Y.; Wang, K.; Chen, N. N. Mineral chemistry and chronology investigation of uraninite in the Jinguanchong uranium deposit in Eastern Hunan province and the implications for geological significance. *ACS Omega* **2024**, *9* (9), 10782−10792.
(72) Pan, C. F.; Ji, Y. L.; Gao, Z. Y.; Zhu, R. K.; Zhu, J. H.; Yu, G. P.; Xu, M. Research on types and development models of Neocene sequences at southern margin of Junggar Basin. *Fault-Block Oil Gas Field* **2011**, *18* (1), 34−37.
(73) Liu, D. G.; Ni, Y. Y.; Chen, J. P.; Li, E. T.; Yao, L. M.; Zhang, Z. H.; et al. Types and sources of crude oil in the Chepaizi uplift, northwest margin of the Junggar Basin. *Acta Geol. Sin.* **2023**, *97* (12), 1576−1597.
(74) Song, Y.; Tang, Y.; He, W. J.; Gong, D. Y.; Yan, Q.; Chen, G.; Gao, G. New fields, new types and exploration potential of oil-gas in the Junggar Basin. *Acta Pet. Sin.* **2024**, *45* (1), 52−68.
(75) Liu, Z. Y.; Peng, S. P.; Qin, M. K.; Huang, S. H.; Geng, Y. Y.; He, Z. B. Constraints on sandstone-type uranium deposits by the tectonic uplift and denudation process in the Eastern Junggar Basin, Northwest China: evidence from apatite fission track and detrital zircon U-Pb Ages. *Minerals* **2022**, *12*, 905.

https://doi.org/10.1021/acsomega.4c07825
ACS Omega 2024, 9, 48681−48696